mathematics

MDPI

Article

A Local Discontinuous Galerkin Formulation for Third-Order Pseudo-Parabolic Problems with Integral Constraints

Nouf A. Alrubea [1], Chandra Pal [2], Ahmed Hussein Msmali [3] and Satyvir Singh [4,5,*]

[1] Department of Mathematics, College of Science, Jouf University, Sakaka 72388, Saudi Arabia; naalswilem@ju.edu.sa
[2] School of Management, IILM University, Greater Noida 201306, Uttar Pradesh, India; chandra@iilm.edu
[3] Department of Mathematics, College of Science, Jazan University, Jazan 45142, Saudi Arabia; amsmali@jazanu.edu.sa
[4] Institute for Applied and Computational Mathematics, RWTH Aachen University, 52062 Aachen, Germany
[5] Department of Mathematics, Graphic Era Deemed to be University, Dehradun 248002, Uttarakhand, India
* Correspondence: singh@acom.rwth-aachen.de; Tel.: +49-1624707356

Abstract

A local discontinuous Galerkin (LDG) formulation is developed for one-dimensional third-order pseudo-parabolic equations with a homogeneous Neumann condition and a zero-integral constraint. The diffusion and mixed space–time terms share one auxiliary gradient, discretized with alternating fluxes and a Legendre modal basis; the constraint becomes a compatible right boundary flux, and sharing the discrete source integral between volume load and flux gives an exact discrete integral law. For compatible initial data and uniquely solvable stage systems, any Runge–Kutta method preserves the zero integral at every stage and step without mean correction; we use the L-stable SDIRK2 method. We prove a semidiscrete energy balance, modal stability for time-dependent coefficients ($a \leq 0$, $|a|$ and b nondecreasing), and an energy-norm estimate of order $h^{p+1/2}$ for Radau-projected initial data; an optimal L^2 estimate remains open. Three manufactured-solution benchmarks show approximately $(p+1)$-order spatial and second-order temporal convergence for the solution, integral residuals below 10^{-12}, and close agreement of discrete and exact energies. The gradient converges at order $p+1$ in the interior, but the first element limits its rate to $p+1/2$ for odd p. For an L^2 error of 10^{-8}, LDG with $p = 4$ needs 76–88 times fewer unknowns than a spline scheme, which is faster in wall time.

Keywords: third-order pseudo-parabolic equations; local discontinuous Galerkin method; nonlocal integral constraints; SDIRK2 time integration; discrete energy stability; constraint preservation

MSC: 65M60; 65M12; 65L06

Check for updates

Academic Editor: Patricia J. Y. Wong

Received: 19 October 2026
Revised: 12 November 2026
Accepted: 17 November 2026
Published: 24 November 2026

Copyright: © 2026 by the authors. Licensee MDPI, Basel, Switzerland. This article is an open access article distributed under the terms and conditions of the Creative Commons Attribution (CC BY) license.

1. Introduction

Pseudo-parabolic equations, also called Sobolev-type equations, are evolution equations in which a mixed space–time derivative is added to a diffusion operator. This term acts as a viscous relaxation of the time derivative. It regularizes the problem and limits how fast high-frequency components of the solution can decay. Showalter and Ting laid the analytical foundations of this class [1]. Such equations arise in models of fluid seepage through fissured rocks [2], in two-temperature theories of heat conduction [3,4], in the propagation of long waves in nonlinear dispersive media [5], and in porous-media flow with dynamic capillary pressure [6]. The present work considers a one-dimensional linear

pseudo-parabolic equation containing the mixed derivative u_{xxt}, which has total differential order three.

In many applications, one classical boundary condition is unavailable and is replaced by a nonlocal condition. A typical example is an integral constraint that prescribes the total mass or mean of the solution over the domain. Integral specifications of this kind go back to Cannon's work on the heat equation with prescribed energy [7], and efficient numerical techniques for parabolic problems with nonlocal specifications have been developed since [8]. For third-order pseudo-parabolic equations, Beshtokov studied nonlocal boundary value problems and built finite-difference schemes for them, including problems with variable and degenerating coefficients [9–11]. Sapagovas and co-workers proposed an alternating-direction implicit method for pseudo-parabolic equations with nonlocal boundary conditions [12]. Inverse problems for third-order pseudo-parabolic models, such as recovering an unknown potential term, have also been investigated [13].

Recent numerical work on the third-order problem with a Neumann condition and an integral constraint uses spline collocation in space and finite differences in time. Dhiman et al. applied a collocation technique and established stability by von Neumann analysis [14]. Meetei et al. used a uniform hyperbolic polynomial B-spline scheme with Crank–Nicolson time stepping (UHPB–CN) and reported second-order convergence in space and time [15]. Being second-order accurate and formulated on uniform meshes, these schemes gain accuracy only by refining both the mesh and the time step. Moreover, a von Neumann analysis alone does not establish stability of the full boundary-value discretization with its nonlocal constraint. The present work instead develops a discontinuous Galerkin formulation in which high spatial accuracy is attained by raising the polynomial degree p, which also admits nonuniform meshes and local variation of h and p, and in which the integral constraint is treated through a boundary flux. For this scheme, we prove a discrete integral law and an energy balance.

Finite element methods for Sobolev and pseudo-parabolic equations have a long history. Ewing analyzed time-stepping Galerkin methods for nonlinear Sobolev equations [16], and Arnold, Douglas and Thomée proved superconvergence of a finite element approximation for the one-dimensional Sobolev equation [17]. Cuesta and Pop developed and analyzed numerical schemes for a pseudo-parabolic Burgers equation with discontinuous data [18]. These works treat classical boundary conditions. For a nonlocal integral constraint, the combination with a high-order finite element or discontinuous Galerkin discretization remains largely unexplored.

Discontinuous Galerkin (DG) methods use piecewise polynomial spaces without inter-element continuity. They offer high-order accuracy, element-local mass matrices, local conservation, and easy variation of mesh size and polynomial degree [19,20]. For second-order operators, Bassi and Rebay introduced a mixed formulation with an auxiliary gradient variable for the compressible Navier–Stokes equations [21]. Arnold, Brezzi, Cockburn and Marini later placed this and related approaches, including interior penalty and lifting-based methods, in a unified framework for elliptic problems [22].

Among these approaches, the local discontinuous Galerkin (LDG) method of Cockburn and Shu [23] is especially well suited to equations with higher-order or mixed derivatives. It rewrites the problem as a first-order system by introducing auxiliary variables for the derivatives. These variables are recovered through elementwise relations involving local mass matrices and numerical traces, and can be eliminated to obtain a system for the primary solution coefficients. A priori error analysis of LDG for elliptic problems was carried out by Castillo et al. [24]. For suitable problems and numerical fluxes, LDG methods admit optimal-order error estimates and superconvergence results in one space dimension [25]. LDG has also been extended to KdV-type and other high-order time-dependent equations [26,27].

Stability and error estimates have been established for LDG discretizations combined with implicit–explicit time integration for advection–diffusion problems [28].

LDG methods have also been applied to Sobolev equations, which share the mixed-derivative structure of pseudo-parabolic equations. Gao, Qiu and Zhang proposed an LDG method with error estimates for a class of Sobolev equations [29], and Zhang and Gao later developed a fully discrete scheme for the convection-dominated case [30]. Zhao and Zhang introduced LDG methods with generalized alternating numerical fluxes for two-dimensional linear Sobolev equations [31], and Abbaszadeh and Dehghan developed an interior penalty DG technique for a generalized Sobolev equation [32]. All of these works assume periodic, compactly supported or Dirichlet data and do not treat a homogeneous Neumann condition combined with a zero-integral constraint. We therefore construct an LDG formulation that ties the nonlocal constraint explicitly to the numerical boundary fluxes and preserves this relation under implicit time integration.

Table 1 summarizes the closest existing approaches. The LDG and DG methods for Sobolev-type equations [29–32] treat periodic, compactly supported or Dirichlet data and contain no nonlocal constraint, whereas the spline and finite-difference methods [9–12,14,15] handle nonlocal conditions, typically at low order and, in the cases we are aware of, on uniform meshes.

Table 1. Closest existing approaches and the present work, compared by spatial discretization, time integration, boundary data or constraints, and available error analysis. UHPB: uniform hyperbolic polynomial B-spline; TVD RKs: explicit total-variation-diminishing Runge–Kutta method of order s; ADI: alternating direction implicit.

Work	Space	Time	Boundary/Constraint	Error Analysis
Beshtokov [9–11]	Finite differences	Implicit	Nonlocal	Yes
Sapagovas et al. [12]	Finite differences	ADI	Nonlocal	Yes
Dhiman et al. [14]	Spline collocation	Finite differences	Neumann + integral	von Neumann
Meetei et al. [15]	UHPB-spline	Crank–Nicolson	Neumann + integral	Numerical
Gao–Qiu–Zhang [29]	LDG, 1D, three auxiliary variables	Semi-discrete; explicit TVD RK2	Periodic or compact support; no constraint	Stability; optimal L^2
Zhang–Gao [30]	LDG, 1D, convection-dominated	Explicit TVD RK3	Periodic or compact support; no constraint	Quasi-optimal/optimal L^2
Zhao–Zhang [31]	LDG, 2D, generalized alternating fluxes	Semi-discrete; explicit TVD RK3	Periodic; no constraint	Weak/strong stability; sharp L^2
Abbaszadeh–Dehghan [32]	Interior-penalty DG (NIPG), 2D	Crank–Nicolson	Dirichlet; no constraint	Semi- and fully discrete
Present work	LDG, Legendre modal, 1D	Any RK; SDIRK2 used	Neumann + integral via boundary flux	Energy, stability, Theorem 1

In this work, we introduce the auxiliary gradient $q = u_x$ and the combined flux $z = \gamma q_t + b(t)q$ (for $b = b(x,t)$, see Remark 6), where $\gamma > 0$ is the pseudo-parabolic parameter and $b(t)$ is the diffusion coefficient. Both the diffusion and mixed space–time derivative terms are discretized using the same LDG gradient operator and complementary alternating numerical fluxes. An orthogonal Legendre modal basis [33] yields diagonal element mass matrices. Moreover, the integral of the discrete solution over each element depends only on its constant mode, allowing exact evaluation of the discrete integral. For compatible initial data, the zero-integral constraint is reformulated as an equivalent right-boundary condition on the combined flux. The numerical boundary flux uses the same discrete source integral as the constant-test-function component of the assembled volume load.

Elimination of the auxiliary variable produces a semidiscrete system with a symmetric positive definite matrix multiplying the time derivative. For small values of γ, the system can exhibit widely separated decay rates. We therefore use Alexander's two-stage,

second-order, L-stable, and stiffly accurate singly diagonally implicit Runge–Kutta method (SDIRK2) [34,35]. With a compatible initial discrete integral and nonsingular stage systems, consistent source and boundary-flux evaluation preserves the zero-integral constraint at each stage. This property follows from the spatial assembly together with the solvability of the stage systems, and holds for any Runge–Kutta method (Proposition 1). SDIRK2 is chosen for its L-stability, which controls the widely separated decay rates for small γ, and for its second-order accuracy with two stages; stiff accuracy is convenient, since the last stage is the completed solution, but it is not required.

Our construction builds on the LDG framework for Sobolev-type equations [29–31], from which we inherit auxiliary variables with alternating numerical fluxes (Table 1). It differs in four respects. (i) Variables: [29–31] use three auxiliary variables ($w = u_t$, $p = w_x$, $q = u_x$; vector-valued in [31]), whereas we use a single auxiliary gradient $q = u_x$ and a combined flux $z = \gamma q_t + b(t)q$ for the diffusion and mixed-derivative terms. (ii) Boundary data: instead of periodic or compactly supported data [29–31] or Dirichlet data [32], we impose the Neumann condition and the zero-integral constraint through a right-boundary flux obtained from the differentiated constraint; the source quadrature shared by the volume load and this flux, with compatible initial data, yields the discrete integral law $I_h' = a(t)I_h$. (iii) Time integration: we use the implicit SDIRK2 scheme instead of explicit TVD Runge–Kutta schemes [29–31] or Crank–Nicolson [32]. (iv) Analysis: [29–31] prove optimal or quasi-optimal L^2 estimates for the solution and [32] prove error estimates for its schemes, whereas we prove an energy-norm estimate of order $h^{p+1/2}$ for (u, q) (Theorem 1); an optimal L^2 estimate for the constrained problem remains open. The LDG framework also underlies error estimates for other equations with higher-order terms [36].

The main contributions of this work are as follows:

- An LDG formulation with alternating numerical fluxes, using a common auxiliary gradient to discretize the diffusion and mixed space–time derivative terms;
- A compatible numerical boundary-flux treatment of the homogeneous left Neumann condition and the zero-integral constraint;
- A derivation of the discrete integral evolution law $I_h' = a(t)I_h$ from the spatial assembly, and a proof that any Runge–Kutta method with uniquely solvable stage systems preserves a zero integral at every stage and completed step, without mean correction;
- A semidiscrete energy balance that mirrors the continuous balance, together with a modal stability analysis of the fully discrete scheme for time-dependent coefficients with $a \leq 0$ and zero forcing, which is unconditional when $|a|$ and b are nondecreasing (Proposition 2);
- An a priori energy-norm error estimate of order $h^{p+1/2}$ for (u, q) (Theorem 1), together with an analysis of the first boundary element that explains the parity-dependent rates of the auxiliary gradient;
- Numerical verification using manufactured solutions, including separate spatial and temporal convergence studies, auxiliary-gradient errors, discrete energy comparisons, and stagewise preservation of the integral constraint;
- A quantitative comparison with the spline scheme UHPB–CN [15]: for an L^2 error of 10^{-8}, roughly 10^2 unknowns for $p = 4$ against roughly 10^4, although UHPB–CN is faster in wall time (Section 4.5).

The remainder of the paper is organized as follows. Section 2 presents the model problem, the compatibility conditions, and the reformulation of the integral constraint as a boundary-flux condition. Section 3 develops the modal LDG discretization and SDIRK2 time integration, together with the energy balance, constraint-preservation results, modal stability analysis, the structure of the stage systems, and an a priori spatial error estimate. Section 4 reports numerical experiments on spatial and temporal accuracy, integral-

constraint preservation, and discrete energy behavior, together with the computational setup and a comparison with the spline scheme UHPB–CN in terms of accuracy and computational cost. Section 5 summarizes the findings and outlines directions for further work.

2. Mathematical Formulation

2.1. Governing Equation

Let $\Omega = (0, L)$, where $L > 0$, denote the spatial domain, and let $T > 0$ be the final time. On the space–time domain $Q_T = \Omega \times (0, T]$, we consider the linear pseudo-parabolic equation

$$u_t - \gamma u_{xxt} - b(t)u_{xx} = a(t)u + f(x,t), \qquad (x,t) \in Q_T, \tag{1}$$

where $\gamma > 0$ is the constant) pseudo-parabolic parameter, $b(t)$ is the diffusion coefficient, $a(t)$ is the reaction coefficient, and $f(x,t)$ is a prescribed source term. Unless otherwise stated, the coefficient functions satisfy

$$a, b \in C^0([0,T]), \qquad b(t) \geq b_{\min} > 0 \quad \text{for all } t \in [0,T]. \tag{2}$$

Here b depends on time only; the case $b = b(x,t)$ is discussed in Remark 6. No sign restriction is imposed on $a(t)$ in the formulation. Additional assumptions needed for stability are stated with the corresponding results.

The designation third-orderrefers to the total differential order of the mixed derivative u_{xxt}. The highest purely spatial derivative in Equation (1) is of second order. Writing Id for the identity operator, the equation takes the operator form

$$(\mathrm{Id} - \gamma\partial_{xx})u_t = b(t)\partial_{xx}u + a(t)u + f(x,t). \tag{3}$$

Thus, a spatial elliptic differential expression acts on the time derivative. This structure motivates a consistent discretization of the spatial derivatives acting on both u and u_t.

The identities below are derived for sufficiently regular solutions. One sufficient regularity class is $u \in C^1([0,T]; H^2(\Omega))$, with $f \in C([0,T]; L^2(\Omega))$ and Equation (1) understood in $L^2(\Omega)$. These assumptions justify the boundary traces, differentiation of the spatial integral, and integration by parts used below; the precise hypotheses are stated in Lemma 1. They are sufficient for the derivations and are not asserted to be minimal.

2.2. Initial and Nonlocal Boundary Conditions

Equation (1) is supplemented by the initial condition

$$u(x,0) = u_0(x), \qquad x \in [0,L], \tag{4}$$

the homogeneous Neumann condition at the left endpoint,

$$u_x(0,t) = 0, \qquad t \in [0,T], \tag{5}$$

and the nonlocal integral constraint

$$I(t) := \int_0^L u(x,t)\,\mathrm{d}x = 0, \qquad t \in [0,T]. \tag{6}$$

The spatial mean is $I(t)/L$; hence, Equation (6) prescribes a zero spatial mean. The numerical experiments use $L = 1$.

The integral constraint supplies global information in place of a separately prescribed local boundary condition at $x = L$. The right boundary contribution must therefore be determined consistently from the governing equation and the integral constraint. In particular, Equation (6) does not imply $u_x(L,t) = 0$.

The initial data $u_0 \in H^2(\Omega)$ must satisfy the compatibility conditions

$$\int_0^L u_0(x)\,\mathrm{d}x = 0, \qquad u_0'(0) = 0, \tag{7}$$

which are Equations (6) and (5) at $t = 0$. Additional compatibility conditions may be required if higher regularity at the space–time corners is imposed.

2.3. Integral Balance and Compatible Right Boundary Flux

Define the integrated source by

$$F(t) := \int_0^L f(x,t)\,\mathrm{d}x. \tag{8}$$

Integrating Equation (1) over Ω gives

$$I'(t) - \gamma[u_{xt}]_0^L - b(t)[u_x]_0^L = a(t)I(t) + F(t), \tag{9}$$

where $[v]_0^L := v(L,t) - v(0,t)$.

Introduce the auxiliary gradient and combined flux

$$q := u_x, \qquad z := \gamma q_t + b(t)q. \tag{10}$$

Because b depends only on time, Equation (1) becomes $u_t - z_x = a(t)u + f$ see Remark 6 for $b = b(x,t)$). The integral balance can therefore also be written as

$$I'(t) = a(t)I(t) + F(t) + z(L,t) - z(0,t). \tag{11}$$

Differentiating Equation (5) in time gives $u_{xt}(0,t) = 0$, and consequently $z(0,t) = 0$. Since the integral constraint implies $I(t) = I'(t) = 0$, Equation (11) reduces to

$$z(L,t) = \gamma u_{xt}(L,t) + b(t)u_x(L,t) = -F(t). \tag{12}$$

This relation specifies the combined right boundary flux, rather than prescribing the right derivative trace independently.

To describe that trace, define

$$g(t) := u_x(L,t). \tag{13}$$

Equation (12) yields

$$\gamma g'(t) + b(t)g(t) = -F(t), \qquad g(0) = u_0'(L). \tag{14}$$

The integrating-factor formula gives

$$\begin{aligned} g(t) &= e^{-B(t)}\left[u_0'(L) - \frac{1}{\gamma}\int_0^t e^{B(s)}F(s)\,\mathrm{d}s\right], \\ B(t) &:= \frac{1}{\gamma}\int_0^t b(s)\,\mathrm{d}s. \end{aligned} \tag{15}$$

Thus, the right derivative trace depends on both the initial profile and the integrated source.

The equivalence between the integral constraint and the compatible right boundary flux is summarized below.

Lemma 1 (Equivalence of the integral constraint and boundary flux)**.** *Let $\gamma > 0$, $\Omega = (0,L)$, $a, b \in C^0([0,T])$ with $b \geq b_{\min} > 0$, $f \in C^0([0,T];L^2(\Omega))$, and $u_0 \in H^2(\Omega)$ with $u_0'(0) = 0$ and $\int_0^L u_0\,\mathrm{d}x = 0$. Let $u \in C^1([0,T];H^2(\Omega))$ satisfy Equation (1) in $L^2(\Omega)$ for every $t \in [0,T]$, together with Equations (4) and (5). Then the integral constraint (6) holds if and only if the right boundary flux satisfies Equation (12).*

Proof. In one space dimension $H^2(\Omega) \subset C^1(\overline{\Omega})$, so u_x and u_{xt} have well-defined traces at $x = 0, L$, and $u_t \in C^0([0,T]; H^2(\Omega))$ gives $\int_0^L u_{xxt}\,\mathrm{d}x = u_{xt}(L,t) - u_{xt}(0,t)$. Moreover $I \in C^1([0,T])$ and $F \in C^0([0,T])$, because $f \in C^0([0,T]; L^2(\Omega)) \subset C^0([0,T]; L^1(\Omega))$. Hence Equation (11) holds for all t, and $z(0,t) = 0$ by Equation (5) and its time derivative.

($\Rightarrow$) If $I \equiv 0$, then $I' \equiv 0$, and Equation (11) gives $z(L,t) = -F(t)$.

($\Leftarrow$) If $z(L,t) = -F(t)$, Equation (11) reduces to

$$I'(t) = a(t)\, I(t). \tag{16}$$

Since $I(0) = 0$, we obtain $I(t) = I(0) \exp\big(\int_0^t a(s)\,\mathrm{d}s\big) = 0$ on $[0,T]$. □

This equivalence provides the continuous foundation for the constraint-preserving numerical boundary flux developed in Section 3.

3. Modal Local Discontinuous Galerkin Method

This section develops a modal local discontinuous Galerkin (LDG) approximation of the linear pseudo-parabolic Equation (1). The spatial discretization uses complementary alternating numerical traces for the solution and combined flux. The same discrete gradient approximates the diffusion and mixed space–time derivative terms. The nonlocal integral constraint is incorporated through a compatible numerical boundary flux. The resulting semidiscrete system is advanced using SDIRK2 time integration.

3.1. Mesh and Modal Approximation Space

Let $\mathcal{T}_h$ be a partition of $\Omega = (0,L)$ defined by

$$\begin{gathered} 0 = x_0 < x_1 < \cdots < x_N = L, \\ K_j = (x_{j-1}, x_j), \qquad h_j = x_j - x_{j-1}, \qquad j = 1, \ldots, N. \end{gathered} \tag{17}$$

We set $h = \max_{1 \le j \le N} h_j$.

For a fixed polynomial degree $p \ge 1$, define

$$V_h^p = \big\{ v_h \in L^2(\Omega) : v_h|_{K_j} \in \mathbb{P}^p(K_j), \quad j = 1, \ldots, N \big\}, \tag{18}$$

where $\mathbb{P}^p(K_j)$ denotes the polynomials of degree at most p on K_j. No continuity is imposed across element interfaces.

Each element is mapped to the reference interval $(-1,1)$ by

$$x = x_{j-\frac{1}{2}} + \frac{h_j}{2}\xi, \qquad x_{j-\frac{1}{2}} = \frac{x_{j-1} + x_j}{2}. \tag{19}$$

Using the standard Legendre polynomials P_k, normalized by $P_k(1) = 1$, we write

$$u_h|_{K_j}(x,t) = \sum_{k=0}^{p} U_{j,k}(t) P_k(\xi(x)). \tag{20}$$

The auxiliary variables use the same basis. Legendre orthogonality gives

$$\int_{K_j} P_k(\xi(x)) P_\ell(\xi(x))\,\mathrm{d}x = \frac{h_j}{2k+1}\delta_{k\ell}, \qquad 0 \le k, \ell \le p, \tag{21}$$

where $\delta_{k\ell}$ is the Kronecker delta. Consequently, the element mass matrices are diagonal.

At an interior interface x_j, define

$$v_h^-(x_j) = \lim_{x \to x_j^-} v_h(x), \qquad v_h^+(x_j) = \lim_{x \to x_j^+} v_h(x), \qquad [v_h]_j = v_h^+(x_j) - v_h^-(x_j). \tag{22}$$

We use $(v,w)_K = \int_K vw\,\mathrm{d}x$ and $(v,w) = \sum_{K \in \mathcal{T}_h} (v,w)_K$. Unless otherwise indicated, $\|\cdot\|$ denotes the $L^2(\Omega)$ norm. The formulation permits nonuniform meshes; all numerical experiments in Section 4 use uniform meshes, and Theorem 1 assumes a quasi-uniform mesh.

3.2. Auxiliary-Variable and Elementwise Weak Formulations

With the auxiliary variables of Equation (10), the governing equation becomes

$$\begin{aligned} q - u_x &= 0, \\ z - \gamma q_t - b(t)\, q &= 0, \\ u_t - z_x &= a(t)\, u + f(x,t), \end{aligned} \tag{23}$$

with the compatible boundary relations $q(0,t) = 0$, $z(0,t) = 0$ and $z(L,t) = -F(t)$, where F is defined in Equation (8).

Let $\Gamma_h = \{x_0, \dots, x_N\}$ be the mesh skeleton. For $K = K_j = (x_{j-1}, x_j)$, a function v with traces $v(x_j^-)$, $v(x_{j-1}^+)$ taken from within K, and a single-valued function $\widehat{w}$ on Γ_h, we write

$$[\widehat{w}\, v]_{\partial K} := \widehat{w}(x_j)\, v(x_j^-) - \widehat{w}(x_{j-1})\, v(x_{j-1}^+).$$

The numerical traces $\hat{u}_h$ and $\hat{z}_h$ are single-valued functions on Γ_h that replace the two-valued traces of u_h and z_h (Equation (22)) in the interface terms. At interior points, they are the alternating traces $\hat{u}_h = u_h^-$ and $\hat{z}_h = z_h^+$; at the physical boundaries, they are given by Equation (27), with F_h defined in Equation (28).

Let $\mathcal{Q}_K$ be the quadrature rule used for the source on element K, and define

$$\mathcal{L}_{K,t}(v_h) := \mathcal{Q}_K[f(\cdot,t)\, v_h].$$

All polynomial inner products below are evaluated exactly; only the source functional uses quadrature.

Multiplying Equation (23) by test functions, integrating by parts on each element and replacing the interface traces by the numerical traces gives the LDG method: find $u_h, q_h, z_h \in V_h^p$ such that, for every $r_h, s_h, v_h \in V_h^p$ and every $K \in \mathcal{T}_h$,

$$(q_h, r_h)_K = -(u_h, \partial_x r_h)_K + [\hat{u}_h\, r_h]_{\partial K}, \tag{24a}$$

$$(z_h, s_h)_K = \gamma(\partial_t q_h, s_h)_K + b(t)\,(q_h, s_h)_K, \tag{24b}$$

$$(\partial_t u_h, v_h)_K + (z_h, \partial_x v_h)_K = a(t)\,(u_h, v_h)_K + \mathcal{L}_{K,t}(v_h) + [\hat{z}_h\, v_h]_{\partial K}. \tag{24c}$$

Only u_h is an evolution variable: Equation (24a) determines q_h algebraically from u_h, Equation (24b) determines z_h from q_h and $\partial_t q_h$, and Equation (24c) then becomes an implicit system for $\partial_t u_h$ (Section 3.4).

3.3. Alternating Numerical Fluxes and Boundary Closure

At every interior interface, we use the alternating numerical traces

$$\hat{u}_h = u_h^-, \qquad \hat{z}_h = z_h^+. \tag{25}$$

This fixed orientation is used throughout the mesh and in all numerical experiments. Here, alternating means that the solution trace and combined-flux trace are selected from opposite sides of each interface; the orientation does not alternate between successive interfaces.

This choice is consistent: when the underlying functions are continuous, the numerical traces equal their physical traces. It also provides the interface cancellation needed for the discrete adjoint relation. In particular, at each interior interface,

$$[v_h w_h]_j = v_h^+ [w_h]_j + w_h^- [v_h]_j. \tag{26}$$

The complementary choices in Equation (25) therefore cancel the interface contributions arising from integration by parts in the gradient and divergence operators.

Since $z_h = \gamma \partial_t q_h + b(t) q_h$, the trace z_h^+ uses the same side for both the diffusion and mixed-derivative contributions. The reverse pairing, $\hat{u}_h = u_h^+$ and $\hat{z}_h = z_h^-$, also has a complementary structure, but it is not used in the reported experiments.

At the physical boundaries, set

$$\begin{aligned} \hat{u}_h(0,t) &= u_h(0^+,t), \quad \hat{u}_h(L,t) = u_h(L^-,t), \\ \hat{z}_h(0,t) &= 0, \qquad\qquad \hat{z}_h(L,t) = -F_h(t). \end{aligned} \tag{27}$$

Here,

$$F_h(t) := \sum_{K\in\mathcal{T}_h} Q_K[f(\cdot,t)] = \sum_{K\in\mathcal{T}_h} \mathcal{L}_{K,t}(1). \tag{28}$$

Thus, the right numerical boundary flux uses exactly the same discrete source integral as the constant-test-function component of the volume load. This algebraic consistency is essential for preserving the integral constraint.

The boundary conditions are imposed through numerical fluxes. In particular, the endpoint values of the auxiliary polynomial q_h are not constrained pointwise. The right numerical flux follows from Equation (12), rather than from an assumption that $q_h(L^-,t) = 0$.

For affine elements, a Gauss–Legendre rule with at least $p+1$ points integrates the polynomial mass and derivative products exactly. Additional points may be needed to evaluate a nonpolynomial source accurately. Regardless of the quadrature order, the same source quadrature must be used in the volume load and in Equation (28). Constraint preservation does not depend on the accuracy of this quadrature, whereas the accuracy of the scheme does.

3.4. Discrete Gradient and Semidiscrete Matrix Formulation

Define the discrete gradient operator $D_h : V_h^p \to V_h^p$ by

$$(D_h v_h, r_h) = -\sum_{K\in\mathcal{T}_h} (v_h, \partial_x r_h)_K + \sum_{K\in\mathcal{T}_h} [\hat{v}_h r_h]_{\partial K}, \qquad r_h \in V_h^p, \tag{29}$$

where $\hat{v}_h = v_h^-$ at interior interfaces and the interior trace is used at each physical boundary. Consequently, $q_h = D_h u_h$.

For the complementary interior trace $\widehat{w}_h = w_h^+$ and prescribed physical boundary fluxes, integration by parts and Equation (26) give

$$\begin{aligned} &\sum_{K\in\mathcal{T}_h} (w_h, \partial_x v_h)_K - \sum_{K\in\mathcal{T}_h} [\widehat{w}_h v_h]_{\partial K} \\ &\qquad = (w_h, D_h v_h) - \widehat{w}_h(L) v_h(L^-) + \widehat{w}_h(0) v_h(0^+). \end{aligned} \tag{30}$$

This identity makes the role of the alternating numerical traces explicit.

Let $\mathbf{U}$ and $\mathbf{Q}$ collect the modal coefficients of u_h and q_h, respectively. The global mass matrix $\mathbf{M}$ is block diagonal with the diagonal entries specified in Equation (21). The discrete gradient relation is

$$\mathbf{MQ} = \mathbf{GU}, \qquad \mathbf{Q} = \mathbf{DU}, \qquad \mathbf{D} := \mathbf{M}^{-1}\mathbf{G}. \tag{31}$$

Here, $\mathbf{D}$ represents D_h. Its evaluation uses element mass-matrix inversions and neighboring solution traces.

Define

$$\mathbf{A} := \mathbf{D}^T\mathbf{MD}. \tag{32}$$

This matrix is symmetric positive semidefinite, since $\mathbf{V}^T\mathbf{AV} = \|D_h v_h\|^2 \geq 0$ for every coefficient vector $\mathbf{V}$ representing v_h.

Because D_h does not depend on time, $\partial_t q_h = D_h \partial_t u_h$, and Equation (24b) gives $z_h = \gamma D_h \partial_t u_h + b(t) D_h u_h$. Using Equation (30) with $w_h = z_h$ and eliminating the auxiliary coefficients yields

$$\mathbf{H}\frac{\mathrm{d}\mathbf{U}}{\mathrm{d}t} = \mathbf{K}(t)\mathbf{U} + \mathbf{R}(t), \tag{33}$$

where

$$\mathbf{H} = \mathbf{M} + \gamma \mathbf{A}, \qquad \mathbf{K}(t) = a(t)\mathbf{M} - b(t)\mathbf{A}. \tag{34}$$

The load vector is specified by

$$\begin{aligned} \mathbf{R}(t) &= \mathbf{f}_h(t) - F_h(t)\boldsymbol{\ell}_R, \\ \mathbf{V}^T \mathbf{f}_h(t) &= \sum_{K \in \mathcal{T}_h} \mathcal{L}_{K,t}(v_h), \\ \boldsymbol{\ell}_R^T \mathbf{V} &= v_h(L^-). \end{aligned} \tag{35}$$

Because $\mathbf{M}$ is symmetric positive definite, $\mathbf{A}$ is symmetric positive semidefinite, and $\gamma > 0$, the matrix $\mathbf{H}$ is symmetric positive definite.

The initial solution is the elementwise L^2 projection of u_0:

$$(u_h(\cdot, 0), v_h)_K = (u_0, v_h)_K, \qquad v_h \in \mathbb{P}^p(K). \tag{36}$$

Let $I_h(t) := \int_0^L u_h(x,t)\,\mathrm{d}x$ denote the discrete integral (see Equation (37)). Testing with $v_h = 1$ shows that exact projection preserves the initial integral. Therefore, Equation (7) implies $I_h(0) = 0$. If projection integrals are evaluated numerically, the initial integral must be checked to the required precision. The initial auxiliary gradient is recovered from $\mathbf{Q}(0) = \mathbf{D}\mathbf{U}(0)$.

3.5. Preservation of the Nonlocal Integral Constraint

By Legendre orthogonality, the discrete integral is

$$I_h(t) := \int_0^L u_h(x,t)\,\mathrm{d}x = \sum_{j=1}^{N} h_j U_{j,0}(t). \tag{37}$$

Taking $v_h = 1$ in Equation (24c) (so that $(z_h, \partial_x 1)_K = 0$) and summing over all elements cancels the single-valued interior numerical fluxes, giving

$$I_h'(t) = a(t) I_h(t) + F_h(t) + \hat{z}_h(L,t) - \hat{z}_h(0,t). \tag{38}$$

Using Equation (27), we obtain

$$I_h'(t) = a(t) I_h(t). \tag{39}$$

Hence, $I_h(0) = 0$ implies $I_h(t) = 0$ in exact arithmetic. This argument relies on single-valued interior fluxes and compatible source–boundary assembly; it does not require exact source integration.

For the matrix formulation, let $\mathbf{c}$ represent the globally constant function 1. Then

$$\mathbf{D}\mathbf{c} = \mathbf{0}, \qquad \mathbf{A}\mathbf{c} = \mathbf{0}, \qquad I_h = \mathbf{c}^T \mathbf{M} \mathbf{U}. \tag{40}$$

Moreover,

$$\mathbf{c}^T \mathbf{R}(t) = \mathbf{c}^T \mathbf{f}_h(t) - F_h(t) = 0, \tag{41}$$

because $\boldsymbol{\ell}_R^T \mathbf{c} = 1$. Since $\mathbf{A}$ is symmetric, $\mathbf{A}\mathbf{c} = \mathbf{0}$ gives $\mathbf{c}^T \mathbf{H} = \mathbf{c}^T \mathbf{M}$ and $\mathbf{c}^T \mathbf{K}(t) = a(t)\,\mathbf{c}^T \mathbf{M}$. Multiplying Equation (33) by $\mathbf{c}^T$ therefore recovers Equation (39). No post-step mean correction is required.

Remark 1 (Quadrature errors)**.** *Constraint preservation does not require exact integration of the source: for any quadrature rule Q_K, $F_h = \sum_K Q_K[f(\cdot,t)]$ is the same functional as the constant-test-function component of the load, so $\mathbf{c}^T \mathbf{R}(t) = 0$ and $I_h' = a\, I_h$ hold identically. What is required is that the* same *rule (nodes, weights and evaluation times) is used for the volume load and for F_h; if the rules differ, I_h is driven by the difference $\sum_K (Q_K^{\mathrm{load}} - Q_K^F)[f(\cdot,t)]$. Quadrature errors do, however, perturb the accuracy: the scheme solves the problem with a perturbed source, and the*

right-boundary flux F_h differs from the exact $F = \int_0^L f\,\mathrm{d}x$ by the quadrature residual measured by E_{compat} (defined in Section 4). For smooth f, this perturbation decreases as the number m of Gauss points increases, and it is below the $O(h^{p+1})$ discretization error once $m \geq p+1$. Quadrature in the initial projection only fixes the initial residual $I_h(0)$, which is then propagated by $I_h' = aI_h$.

3.6. Continuous and Semidiscrete Energy Balances

For sufficiently regular continuous solutions satisfying the compatible boundary conditions, integration by parts gives

$$(u_t, v) + \gamma(u_{xt}, v_x) + b(t)(u_x, v_x) = a(t)(u, v) + (f, v) - F(t)v(L), \qquad v \in H^1(\Omega). \tag{42}$$

Taking $v = u$ yields

$$\begin{aligned} \frac{\mathrm{d}}{\mathrm{d}t}\mathcal{E}(t) + b(t)\|u_x\|^2 &= a(t)\|u\|^2 + (f, u) - F(t)u(L, t), \\ \mathcal{E}(t) &:= \frac{1}{2}\big(\|u\|^2 + \gamma\|u_x\|^2\big). \end{aligned} \tag{43}$$

For the LDG approximation, define

$$\mathcal{E}_h(t) := \frac{1}{2}\mathbf{U}^T\mathbf{H}\mathbf{U} = \frac{1}{2}\big(\|u_h\|^2 + \gamma\|q_h\|^2\big). \tag{44}$$

Multiplication of Equation (33) by $\mathbf{U}^T$ gives

$$\begin{aligned} \frac{\mathrm{d}}{\mathrm{d}t}\mathcal{E}_h(t) + b(t)\|q_h\|^2 = a(t)\|u_h\|^2 &+ \sum_{K\in\mathcal{J}_h} \mathcal{L}_{K,t}(u_h) \\ &- F_h(t)u_h(L^-, t). \end{aligned} \tag{45}$$

Thus, the discrete energy balance retains both the volume-source contribution and the compatible right boundary contribution.

For $f = 0$ and $a(t) \leq 0$, both $\mathcal{L}_{K,t}(\cdot)$ and F_h vanish, so Equation (45) reduces to $\mathcal{E}_h' = a(t)\|u_h\|^2 - b(t)\|q_h\|^2 \leq 0$, and $\mathcal{E}_h(t)$ is nonincreasing. In this homogeneous case, the same estimate applies to the difference between two semidiscrete solutions with identical data, establishing stability with respect to initial perturbations in the $\mathbf{H}$-norm $\|\mathbf{V}\|_{\mathbf{H}}^2 := \mathbf{V}^T\mathbf{H}\mathbf{V}$. The energy identity alone does not give a spatial error estimate; an energy-norm estimate is established in Section 3.9.

3.7. SDIRK2 Time Integration

Let t_n be the current time and $\Delta t = t_{n+1} - t_n$. We advance Equation (33) using Alexander's two-stage, second-order, L-stable, stiffly accurate SDIRK2 method [34,35], whose Butcher tableau is

$$\begin{array}{c|cc} \theta & \theta & 0 \\ 1 & 1-\theta & \theta \\ \hline & 1-\theta & \theta \end{array}, \qquad \theta = 1 - \frac{1}{\sqrt{2}}. \tag{46}$$

The stage times are

$$t_{n,1} = t_n + \theta\Delta t, \qquad t_{n,2} = t_n + \Delta t. \tag{47}$$

Let $\mathbf{Y}_i$ denote the stage solution and $\mathbf{k}_i$ the corresponding approximation to the time derivative. The stage equations are

$$\begin{aligned} \mathbf{Y}_i &= \mathbf{U}^n + \Delta t \sum_{j=1}^{i} \alpha_{ij}\mathbf{k}_j, \\ \mathbf{H}\mathbf{k}_i &= \mathbf{K}(t_{n,i})\mathbf{Y}_i + \mathbf{R}(t_{n,i}), \qquad i = 1, 2, \end{aligned} \tag{48}$$

where $\alpha_{11} = \alpha_{22} = \theta$, $\alpha_{21} = 1-\theta$, and $\alpha_{12} = 0$. The notation α_{ij} distinguishes the Runge–Kutta coefficients from the reaction coefficient $a(t)$.

The first stage satisfies

$$\big[\mathbf{H} - \theta\Delta t\,\mathbf{K}(t_{n,1})\big]\mathbf{Y}_1 = \mathbf{H}\mathbf{U}^n + \theta\Delta t\,\mathbf{R}(t_{n,1}), \tag{49}$$

after which

$$\mathbf{k}_1 = \frac{\mathbf{Y}_1 - \mathbf{U}^n}{\theta\Delta t}. \tag{50}$$

The second stage satisfies

$$\begin{aligned}\big[\mathbf{H} - \theta\Delta t\,\mathbf{K}(t_{n,2})\big]\mathbf{Y}_2 = \mathbf{H}\mathbf{U}^n + (1-\theta)\Delta t\,\mathbf{H}\mathbf{k}_1 \\ + \theta\Delta t\,\mathbf{R}(t_{n,2}).\end{aligned} \tag{51}$$

The second-stage derivative and completed solution are

$$\mathbf{k}_2 = \frac{\mathbf{Y}_2 - \mathbf{U}^n - (1-\theta)\Delta t\,\mathbf{k}_1}{\theta\Delta t}, \qquad \mathbf{U}^{n+1} = \mathbf{Y}_2. \tag{52}$$

At each stage, the coefficients, source load, and numerical boundary flux are evaluated at the same stage time. The auxiliary coefficients are recovered as

$$\begin{aligned}\mathbf{Q}_i &= \mathbf{D}\mathbf{Y}_i, \\ \mathbf{Z}_i &= \gamma\mathbf{D}\mathbf{k}_i + b(t_{n,i})\mathbf{Q}_i, \\ \hat{z}_h(0,t_{n,i}) = 0, &\qquad \hat{z}_h(L,t_{n,i}) = -F_h(t_{n,i}).\end{aligned} \tag{53}$$

The prescribed numerical boundary values in Equation (53) are distinct from the interior endpoint values of the polynomial represented by $\mathbf{Z}_i$.

The stage matrix has the structure

$$\begin{aligned}\mathbf{H} - \theta\Delta t\,\mathbf{K}(t) = [1 - \theta\Delta t\,a(t)]\mathbf{M} \\ + [\gamma + \theta\Delta t\,b(t)]\mathbf{A}.\end{aligned} \tag{54}$$

It is symmetric positive definite if $1 - \theta\Delta t\,a(t) > 0$. This condition holds for every positive time step when $a(t) \le 0$.

Denote $\mathbf{S}_i := \mathbf{H} - \theta\Delta t\,\mathbf{K}(t_{n,i})$, $i = 1,2$. Since $\mathbf{M}$ is diagonal and, with the alternating fluxes (25), $\mathbf{D}$ couples each element K_j only with K_{j-1}, $\mathbf{A} = \mathbf{D}^T\mathbf{M}\mathbf{D}$ is block tridiagonal with blocks of size $(p+1)\times(p+1)$. Hence $\mathbf{S}_i$ is symmetric and block tridiagonal with $N(p+1)$ unknowns, and positive definite under the condition of Lemma 2.

Remark 2 (Stiffness for small γ)**.** *The modal decay rates $b\lambda_j/(1+\gamma\lambda_j)$ approach b/γ as $\lambda_j \to \infty$, so the rates range from $O(b)$ to $O(b/\gamma)$, independently of h. This spread motivates an L-stable method such as SDIRK2; for moderate γ an explicit method is also stable under a step restriction (Section 4.5).*

Lemma 2 (Solvability of the SDIRK2 stages)**.** *Let $\theta = 1 - 1/\sqrt{2}$. If $\theta\Delta t\,a(t_{n,i}) < 1$, $i = 1,2$ (e.g., $\Delta t < (2+\sqrt{2})/a_{\max}$; no restriction if $a \le 0$), the stage matrices $\mathbf{S}_i = [1 - \theta\Delta t\,a(t_{n,i})]\mathbf{M} + [\gamma + \theta\Delta t\,b(t_{n,i})]\mathbf{A}$ are symmetric positive definite and the stage systems (49), (51) are uniquely solvable. The condition is sharp for positive definiteness, since $\mathbf{c}^T\mathbf{S}_i\mathbf{c} = [1 - \theta\Delta t\,a(t_{n,i})]\,\mathbf{c}^T\mathbf{M}\mathbf{c}$.*

Proof. $\mathbf{S}_i = \alpha_i\mathbf{M} + \beta_i\mathbf{A}$ with $\alpha_i, \beta_i > 0$, $\mathbf{M}$ positive definite and $\mathbf{A}$ positive semidefinite; stage 2 involves only $\mathbf{U}^n$, $\mathbf{k}_1$ and $\mathbf{R}(t_{n,2})$. □

3.8. Fully Discrete Constraint Preservation and Linear Stability

Define the completed-step and stage integrals by

$$I_h^n := \mathbf{c}^T \mathbf{M} \mathbf{U}^n, \qquad I_h^{n,i} := \mathbf{c}^T \mathbf{M} \mathbf{Y}_i, \qquad i = 1, 2. \tag{55}$$

Using Equations (40) and (41) in the stage equations gives

$$I_h^{n,i} = I_h^n + \Delta t \sum_{j=1}^{i} \alpha_{ij} a(t_{n,j}) I_h^{n,j}. \tag{56}$$

In particular,

$$\begin{aligned} \left[1 - \theta \Delta t\, a(t_{n,1})\right] I_h^{n,1} &= I_h^n, \\ \left[1 - \theta \Delta t\, a(t_{n,2})\right] I_h^{n,2} &= I_h^n + (1-\theta)\Delta t\, a(t_{n,1}) I_h^{n,1}. \end{aligned} \tag{57}$$

If $I_h^n = 0$ and both stage systems are nonsingular, the scalar factors on the left are nonzero. Indeed, a zero factor would make the corresponding stage matrix annihilate the constant vector $\mathbf{c}$. Equation (57) therefore implies $I_h^{n,1} = I_h^{n,2} = 0$. Stiff accuracy gives $I_h^{n+1} = I_h^{n,2} = 0$.

Starting from $I_h^0 = 0$, the integral constraint is thus preserved at every stage and completed time step in exact arithmetic. In computations, the residual depends on the initial projection, source–boundary assembly, floating-point roundoff, and linear-solver tolerances.

Proposition 1 (General Runge–Kutta methods)**.** *Apply a Runge–Kutta method with coefficients α_{ij} and weights ω_i to Equation (33), with a, b, the load and the boundary flux evaluated at the stage times $t_{n,i}$. If $I_h^n = 0$ and the coupled stage system is uniquely solvable, then $I_h^{n,i} = 0$ for all stages and $I_h^{n+1} = 0$.*

Proof. By Equations (40) and (41), multiplying the stage equation by $\mathbf{c}^T$ gives $\mathbf{c}^T \mathbf{M} \mathbf{k}_i = a_i I_h^{n,i}$, so the stage integrals satisfy $\mathbf{I} = I_h^n \mathbf{1} + \Delta t\, \mathcal{A}\, \mathrm{diag}(a_i)\, \mathbf{I}$. If $\boldsymbol{\iota} \neq \mathbf{0}$ solved the homogeneous system, then $\mathbf{k}_j = a_j \iota_j \mathbf{c}$ (not all zero, since otherwise $\boldsymbol{\iota} = \mathbf{0}$) would be a nonzero solution of the homogeneous coupled stage system, because $\mathbf{H}\mathbf{c} = \mathbf{M}\mathbf{c}$ and $\mathbf{K}(t_{n,i})\mathbf{c} = a_i \mathbf{M}\mathbf{c}$; this contradicts unique solvability. Hence $\mathbf{I} = \mathbf{0}$ and $I_h^{n+1} = I_h^n + \Delta t \sum_i \omega_i a_i I_h^{n,i} = 0$. □

Remark 3. *Constraint preservation is a property of the spatial assembly, Equations (39)–(41), together with solvability of the stage systems (Lemma 2). Stiff accuracy is convenient, because the last stage then equals the completed solution (Equations (56) and (57)), but it is not necessary. SDIRK2 is chosen for its L-stability, which controls the widely separated decay rates for small γ, and for its second-order accuracy with two stages. Since I_h is the amplitude of the constant mode ($\lambda = 0$ below), an initial residual $I_h^0 \neq 0$ is advanced by the Runge–Kutta recursion for $I_h' = a(t) I_h$; for $a \leq 0$ it does not grow under the condition of Proposition 2.*

Let $\mathbf{A}\mathbf{v} = \lambda \mathbf{M}\mathbf{v}$ be the generalized eigenproblem. Since $\mathbf{M}$ is symmetric positive definite and $\mathbf{A}$ symmetric positive semidefinite, an $\mathbf{M}$-orthonormal eigenbasis $\{\mathbf{v}_j\}$ with $\lambda_j \geq 0$ exists. It diagonalizes $\mathbf{H} = \mathbf{M} + \gamma \mathbf{A}$ and $\mathbf{K}(t) = a(t)\mathbf{M} - b(t)\mathbf{A}$ for every t, because a and b are scalar functions of time. With $f = 0$, each modal coefficient satisfies

$$y_j' = \rho_j(t)\, y_j, \qquad \rho_j(t) = \frac{a(t) - b(t)\lambda_j}{1 + \gamma \lambda_j}. \tag{58}$$

Let $\theta = 1 - 1/\sqrt{2}$ and $\sigma = 1 - 2\theta = \sqrt{2} - 1$. One SDIRK2 step maps y_j^n to $R_j^n y_j^n$ with

$$R_j^n = \frac{1 + \sigma z_1}{(1 - \theta z_1)(1 - \theta z_2)}, \qquad z_i = \Delta t\, \rho_j(t_{n,i}). \tag{59}$$

For constant coefficients, $z_1 = z_2$, and this reduces to the classical stability function, so the method is A-stable and L-stable [34,35].

Proposition 2 (Modal stability for time-dependent coefficients)**.** *Let $a(t) \le 0$, $b(t) \ge b_{\min} > 0$ and $f = 0$. If $|a(t_{n+1})| \ge (\sqrt{2}-1)\,|a(t_{n,1})|$ and $b(t_{n+1}) \ge (\sqrt{2}-1)\,b(t_{n,1})$, then $|R_j^n| \le 1$ for all j, and the discrete energy $E_h^n = \frac{1}{2}(\mathbf{U}^n)^T \mathbf{H}\,\mathbf{U}^n = \frac{1}{2}\sum_j (1+\gamma\lambda_j)(y_j^n)^2$ is nonincreasing. In particular, no restriction on Δt arises if $|a|$ and b are nondecreasing.*

Proof. With $w_i = -z_i \ge 0$, $|R_j^n| \le 1$ is equivalent to $|1-\sigma w_1| \le (1+\theta w_1)(1+\theta w_2)$. If $\sigma w_1 \le 1$, the left side is at most 1. Otherwise, $w_i = \Delta t\,(|a(t_{n,i})|+b(t_{n,i})\lambda_j)/(1+\gamma\lambda_j)$ and the hypotheses give $w_2 \ge \sigma w_1$, so the right side is at least $1+\theta(1+\sigma)w_1 = 1+\theta\sqrt{2}\,w_1 = 1+\sigma w_1 \ge \sigma w_1 - 1$. □

Examples 2 and 3 satisfy the hypothesis for every Δt. For $a > 0$ (Example 1), the continuous problem can grow for modes with $\lambda_j < a/b$, so no decay claim is made. The source term enters as an inhomogeneity and does not change the amplification factors, which govern the propagation of initial perturbations. Spatial convergence and integral-constraint preservation are examined in Section 4.

3.9. A Priori Spatial Error Estimate

Let P_h be the elementwise L^2 projection of Equation (36). Define the Gauss–Radau projections $P^{\pm}$ by

$$(w - P^{\pm}w, r)_K = 0, \qquad r \in \mathbb{P}^{p-1}(K),$$

with

$$(P^- w)(x_j^-) = w(x_j), \qquad (P^+ w)(x_{j-1}^+) = w(x_{j-1}).$$

For $v_h \in V_h^p$, write

$$\|v_h\|_{h,\gamma}^2 = \|v_h\|^2 + \gamma\|D_h v_h\|^2.$$

Theorem 1. *Let $\gamma > 0$, $p \ge 1$, and $a, b \in C([0,T])$ with $b \ge b_{\min} > 0$, and let the mesh be quasi-uniform. Let u be the solution of the model problem with the compatible initial and boundary data of Section 2. Assume exact source integration and $u \in C^1([0,T]; H^{p+2}(\Omega))$. Set*

$$\mathcal{M} = \|u\|_{L^\infty(0,T;H^{p+2})} + \|u_t\|_{L^\infty(0,T;H^{p+2})}.$$

Then,

$$\begin{aligned} &\sup_{t\le T}\Big(\|u-u_h\| + \sqrt{\gamma}\|q-q_h\|\Big) + \left(\int_0^T b\|q-q_h\|^2\,\mathrm{d}t\right)^{1/2} \\ &\qquad \le C\Big[\|P^- u_0 - u_h(0)\|_{h,\gamma} + (1+\sqrt{\gamma}+\gamma)h^{p+1/2}\mathcal{M}\Big]. \end{aligned} \tag{60}$$

The constant C depends on p, mesh quasi-uniformity, L, T, $b_{\min}^{-1}$, and bounds on $|a|$ and b, but not on h or γ. For $u_h(0) = P^- u_0$, the initial term vanishes. For $u_h(0) = P_h u_0$, it is bounded by

$$C\Big(h^{p+1} + \sqrt{\gamma}h^p\Big)\|u_0\|_{H^{p+1}(\Omega)}.$$

Proof. Set $w_h = P^- u$, $\eta = u - w_h$, and $\delta_0 = \eta(0^+, t)$. Let $\mathcal{L}_0 \in V_h^p$ be supported on K_1 and satisfy

$$(\mathcal{L}_0, r_h)_{K_1} = r_h(0^+), \qquad r_h \in \mathbb{P}^p(K_1).$$

Projection orthogonality cancels the volume terms in the gradient relation. The right-endpoint interpolation cancels all trace defects except at $x = 0$, where the closure uses $w_h(0^+)$. Hence,

$$(D_h w_h - q, r_h) = \delta_0 r_h(0^+), \qquad D_h P^- u = P_h q + \delta_0 \mathcal{L}_0.$$

Legendre orthogonality gives $\|\mathcal{L}_0\|_{K_1} = (p+1)h_1^{-1/2}$. The endpoint approximation estimate and the one-dimensional embedding $H^{p+2}(\Omega) \hookrightarrow W^{p+1,\infty}(\Omega)$ give

$$|\delta_0| \le Ch_1^{p+1}\|u\|_{W^{p+1,\infty}(K_1)} \le Ch_1^{p+1}\|u\|_{H^{p+2}(\Omega)}.$$

Thus, for $s_h = P^+q - D_h w_h$ and sufficiently small h,

$$\begin{aligned} \|s_h\| &\le Ch^{p+1/2}\|u\|_{H^{p+2}}, \quad \|s_{h,t}\| \le Ch^{p+1/2}\|u_t\|_{H^{p+2}}, \\ \|\eta\| &\le Ch^{p+1}\|u\|_{H^{p+1}}, \qquad \|\eta_t\| \le Ch^{p+1}\|u_t\|_{H^{p+1}}. \end{aligned} \tag{61}$$

The moments and left-endpoint interpolation of P^+ imply

$$(P^+z, D_h v_h) = \sum_K (z, \partial_x v_h)_K + \sum_{j=1}^{N-1} z(x_j)[v_h]_j.$$

Integrating the continuous equation elementwise therefore gives

$$(u_t, v_h) + (P^+z, D_h v_h) = a(u, v_h) + (f, v_h) - Fv_h(L^-).$$

Under exact integration, the semidiscrete equation contains the same prescribed boundary term $-Fv_h(L^-)$, so it cancels upon subtraction. No condition on $(P^+z)(L^-)$ is required.

Set $e_h = w_h - u_h$. Since $b = b(t)$,

$$P^+z = \gamma D_h w_{h,t} + bD_h w_h + \gamma s_{h,t} + bs_h.$$

Subtracting the semidiscrete equation yields

$$\begin{aligned} (e_{h,t}, v_h) + \gamma(D_h e_{h,t}, D_h v_h) + b(D_h e_h, D_h v_h) &= a(e_h, v_h) \\ &\quad + (a\eta - \eta_t, v_h) - (\gamma s_{h,t} + bs_h, D_h v_h). \end{aligned} \tag{62}$$

Taking $v_h = e_h$, setting $E_e = \frac{1}{2}\|e_h\|^2_{h,\gamma}$, and applying Young's inequality gives

$$E_e' + \frac{b}{2}\|D_h e_h\|^2 \le CE_e + C\left(\|\eta\|^2 + \|\eta_t\|^2 + b\|s_h\|^2 + \frac{\gamma^2}{b}\|s_{h,t}\|^2\right).$$

Gronwall's inequality and Equation (61) imply

$$\sup_{t\le T}\|e_h(t)\|^2_{h,\gamma} + \int_0^T b\|D_h e_h\|^2\,\mathrm{d}t \le C\left[\|e_h(0)\|^2_{h,\gamma} + (1+\gamma^2)h^{2p+1}\mathcal{M}^2\right].$$

Using

$$u - u_h = \eta + e_h, \qquad q - q_h = (q - P^+q) + s_h + D_h e_h$$

proves Equation (60).

For $u_h(0) = P^-u_0$, $e_h(0) = 0$. For $u_h(0) = P_h u_0$, approximation and the discrete inverse estimate $\|D_h v_h\| \le Ch^{-1}\|v_h\|$, which follows from polynomial inverse and trace inequalities on the quasi-uniform mesh, give

$$\|e_h(0)\| \le Ch^{p+1}\|u_0\|_{H^{p+1}}, \qquad \|D_h e_h(0)\| \le Ch^p\|u_0\|_{H^{p+1}},$$

which proves the stated initial-data contribution. □

Remark 4 (Boundary closure and parameter dependence)**.** *On K_1, both solution traces come from K_1, so $q_h = \partial_x u_h \in \mathbb{P}^{p-1}(K_1)$. Consequently,*

$$\|q - q_h\|_{K_1} \ge \mathrm{dist}_{L^2(K_1)}\left(q, \mathbb{P}^{p-1}(K_1)\right).$$

For sufficiently smooth u with $u^{(p+1)}(0,t) \neq 0$, this best-approximation error has leading order $h_1^{p+1/2}$. Its leading coefficient vanishes for even p when u is even about $x = 0$. The corresponding physical-boundary defect is absent in the periodic projection argument, so standard periodic LDG analyses [24,25,29–31] do not transfer directly. An optimal-order L^2 estimate remains open.

The estimate is uniform for $0 < \gamma \le \gamma_{\max}$ provided the coefficient bounds and solution regularity norms remain uniform. It controls the pointwise gradient with weight $\sqrt{\gamma}$, not the unweighted pointwise gradient. No inverse power of γ is introduced in the energy argument because the consistency terms are absorbed using $b \ge b_{\min} > 0$.

Remark 5 (Quadrature). *With numerical source quadrature, Equation (62) contains the additional functional*

$$(f, v_h) - \sum_K L_{K,t}(v_h) + (F_h - F)v_h(L^-),$$

which requires a separate consistency bound. Shared source–boundary quadrature preserves the integral law but does not eliminate solution error due to quadrature.

Remark 6 (Spatially varying diffusion). *For conservative diffusion $(b(x,t)u_x)_x$, with continuous $b \geq b_{\min} > 0$, use $z = \gamma q_t + b(x,t)q$ and replace Equation (24b) by*

$$(z_h, s_h)_K = \gamma(\partial_t q_h, s_h)_K + (bq_h, s_h)_K.$$

The numerical traces in Equations (25) and (27) are unchanged. Under sufficient regularity, Lemma 1 and Proposition 1 remain valid, with $b(L,t)$ replacing $b(t)$ in Equations (14) and (15). The diffusion matrix becomes $\mathbf{D}^T\mathbf{M}_b(t)\mathbf{D}$. Proposition 2 and Theorem 1 do not apply directly: the common-eigenbasis argument and the identity $P^+(bq) = b(t)P^+q$ are no longer available.

For non-conservative diffusion $b\,u_{xx}$, the identity $b\,u_{xx} = (bq)_x - b_x q$ introduces a volume term and requires a nonlocal correction to the right boundary flux. This extension is left for future work.

4. Numerical Results and Discussion

We assess the LDG–SDIRK2 scheme using three manufactured solutions on $\Omega = (0,1)$ that satisfy the homogeneous left Neumann condition and the zero-integral constraint. Examples 1 and 2 have polynomial and trigonometric solutions, respectively, whereas Example 3 combines both components with a time-dependent, nonzero right boundary flux.

4.1. Computational Setup and Error Measures

For each exact solution u, the source and initial data are

$$f(x,t) = u_t - \gamma u_{xxt} - b(t)\,u_{xx} - a(t)\,u, \tag{63a}$$

$$u_0(x) = u(x,0). \tag{63b}$$

All computations use the alternating traces $\hat{u}_h = u_h^-$, $\hat{z}_h = z_h^+$ at interior interfaces and the boundary fluxes

$$\hat{z}_h(0,t) = 0, \qquad \hat{z}_h(1,t) = -F_h(t), \tag{64}$$

with F_h assembled by the same source quadrature as the volume load. The initial solution is the elementwise L^2 projection of u_0, and no mean correction or extrapolation is applied. The number of primary unknowns is $N_{\text{dof}} = N(p+1)$. The rate $h^{p+1/2}$ in Theorem 1 corresponds to Radau-projected initial data. For the L^2 projection used here, the estimate additionally contains $C(h^{p+1} + \sqrt{\gamma}h^p)$. For fixed $\gamma > 0$, the h^p term is the lower-order contribution as $h \to 0$; when γ also varies, its relative importance depends on the relation between h and γ.

For $e_h = u_h - u$, the errors are

$$\begin{aligned} E_{L^2}(t) &= \Big(\sum_{K\in\mathcal{T}_h}\int_K |e_h|^2\,\mathrm{d}x\Big)^{1/2}, \\ E_{L^\infty}(t) &= \max_{K\in\mathcal{T}_h}\sup_{x\in\overline{K}} |e_h(x,t)|, \\ E_{q,L^2}(t) &= \|q_h - u_x\|_{L^2(\Omega)}, \end{aligned} \tag{65}$$

where E_{L^∞} includes both one-sided interface traces. Convergence rates are computed from unrounded errors as

$$r_h = \frac{\log(E_N/E_{2N})}{\log 2}, \qquad r_t = \frac{\log(E_{\Delta t}/E_{\Delta t/2})}{\log 2}, \tag{66}$$

where E_N is the error on N elements and $E_{\Delta t}$ the error with time step Δt.

After confirming second-order temporal convergence, the temporal error in the spatial refinement studies is controlled by step doubling: the finer solution is accepted when

$$\frac{\|u_h^{\Delta t/2}(T) - u_h^{\Delta t}(T)\|_{L^r(\Omega)}}{3} \le 0.1\, E_{L^r}^{\Delta t/2}(T), \qquad r = 2, \infty, \tag{67}$$

and the same test is applied to the auxiliary-gradient L^2-error. Spatial rates are interpreted only when this criterion holds. For Example 1, the quadratic solution is reproduced exactly for $p \ge 2$, so spatial rates are reported only for $p = 1$. In Example 2 with $\gamma = b = 1$, the spatial terms cancel for the exact solution; Example 3 provides a test without this cancellation.

Time steps. In the spatial refinement studies, Δt starts at 0.01 and is halved until Equation (67) holds and the error ratio on halving lies in $[3.5, 4.5]$; the accepted values ($\Delta t \le 2.5 \times 10^{-3}$) are listed in the tables. In the fixed-step tables Δt is given in the caption; for Example 1 the error is purely temporal, so Equation (67) is not meaningful and $\Delta t = 6.25 \times 10^{-4}$ keeps the temporal error below 3×10^{-8}.

The constraint is monitored through the completed-step and stage integrals, evaluated from the constant Legendre modes,

$$I_h^n = \sum_{j=1}^{N} h_j U_{j,0}^n, \qquad I_h^{n,i} = \sum_{j=1}^{N} h_j (\mathbf{Y}_i)_{j,0}, \tag{68}$$

with maximum residuals

$$E_{\text{mean}} = \max_n |I_h^n|, \qquad E_{\text{stage}} = \max_{n,i} |I_h^{n,i}|. \tag{69}$$

With the exact right boundary flux $z_R(t) := \gamma u_{xt}(1,t) + b(t) u_x(1,t)$, data compatibility and the assembled flux balance are measured separately by

$$\begin{aligned} E_{\text{compat}} &= \max_{n,i} \left| F_h(t_{n,i}) + z_R(t_{n,i}) \right|, \\ E_{\text{balance}} &= \max_{n,i} \left| \mathbf{c}^T \mathbf{R}(t_{n,i}) \right| = \max_{n,i} \left| \mathbf{c}^T \mathbf{f}_h(t_{n,i}) - F_h(t_{n,i}) \right|. \end{aligned} \tag{70}$$

For compatible data, E_{compat} reflects the source quadrature error and roundoff in F_h and z_R, while E_{balance} vanishes in exact arithmetic by Equation (41).

Implementation. Computations use Python 3.13 (NumPy 2.5, SciPy 1.18) on a single thread of a laptop with an 11th Gen Intel Core i3-1115G4 CPU (2 cores, 4 logical processors, 3.00 GHz base clock), 16 GiB RAM and Windows 11 Enterprise. On each element, a 12-point Gauss–Legendre rule is used for the source load, F_h and the initial projection, and a 20-point rule for the L^2-errors. We estimate the L^∞-error by evaluating $|e_h|$ at 201 equispaced points per element, including both one-sided traces at each interior interface, and refining the maximum estimate with a local search. In every case, the maximum occurred at an element endpoint, and doubling or quadrupling the sampling density left its value unchanged. The block-tridiagonal stage matrices $\mathbf{S}_i$ (Section 3.7) are factorized at every stage by a sparse LU (SuperLU), since $a(t)$ and $b(t)$ vary in time; the backward error of every solve is at most 1.4×10^{-16}. The estimated condition number ranges from about 8×10^1 to 1.4×10^6 and grows like h^{-2}, with $\kappa(\mathbf{M}^{-1}\mathbf{S}_i) \lesssim 1 + (\gamma + \theta \Delta t\, b)\, C_p / h_{\min}^2$, so it does not deteriorate as $\gamma \to 0$.

Solvability of the stages. By Lemma 2, the stage matrices are symmetric positive definite if $\theta \Delta t\, a(t_{n,i}) < 1$. In Examples 2 and 3, $a(t) = -(1 + 2t)$ and $a(t) = -1$, so no restriction on Δt applies; moreover $b = 1$ and $|a| = 1 + 2t$ in Example 2, and $b = 1 + t$ and $|a| = 1$ in Example 3, so $|a|$ and b are nondecreasing and Proposition 2 holds for every Δt. In Example 1, $a(t) = 1 + t$ with $\max_{[0,1]} a = 2$, so the condition reads $\Delta t < 1/(2\theta) \approx 1.707$, and this example lies outside the scope of Proposition 2. The largest time step used in any run is $\Delta t = 0.2$, giving $\theta \Delta t \max a = 0.117$; for the convergence studies ($\Delta t \le 0.05$), $\theta \Delta t \max a \le 0.03$.

4.2. Example 1: Polynomial Manufactured Solution

On $(x,t) \in [0,1] \times [0,1]$, consider the exact solution and initial data

$$u(x,t) = e^t\left(\frac{1}{3} - x^2\right), \qquad u_0(x) = \frac{1}{3} - x^2. \tag{71}$$

For $\gamma = 1$ and $a(t) = b(t) = 1 + t$, Equation (63a) gives

$$f(x,t) = e^t\left[t\left(x^2 - \frac{1}{3}\right) + 4 + 2t\right]. \tag{72}$$

The solution satisfies $u_x(0,t) = 0$ and $\int_0^1 u\,\mathrm{d}x = 0$. Since $u_x(1,t) = -2e^t$, the combined right boundary flux is

$$z_R(t) = \gamma u_{xt}(1,t) + b(t)u_x(1,t) = -(4+2t)e^t, \tag{73}$$

and the integrated source is

$$F(t) = \int_0^1 f(x,t)\,\mathrm{d}x = (4+2t)e^t. \tag{74}$$

Hence, $z_R(t) + F(t) = 0$, consistent with Lemma 1, and the example tests the nonzero right boundary flux required by the integral constraint. For $p \geq 2$ the quadratic solution and its gradient belong to the approximation space, so with exact initial projection and integration the scheme reproduces it in space, leaving temporal and roundoff errors. Spatial convergence is therefore assessed only for $p = 1$.

Figure 1 shows that the LDG profiles follow the exact ones. The solution keeps its quadratic shape with amplitude growing like e^t and changes sign at $x = 1/\sqrt{3}$, whereas $q = -2xe^t$ is linear and vanishes at $x = 0$. Its nonzero value at $x = 1$ shows that the zero-integral constraint does not imply a homogeneous right Neumann condition.

Figure 2 shows both errors growing with time. The solution error has a minimum near $x = 1/\sqrt{3}$, where u vanishes, and the gradient error increases toward $x = 1$; this is consistent with a temporal amplitude error in a spatially reproduced polynomial. Table 2 confirms this at $T = 1$: the solution errors lie between 1.55×10^{-10} (at $x = 0.6$, near the zero crossing) and 8.90×10^{-9}, and the gradient errors between 3.77×10^{-13} (at $x = 0$) and 2.99×10^{-8} (at $x = 1$). These runs therefore assess temporal accuracy and polynomial reproduction, not spatial convergence.

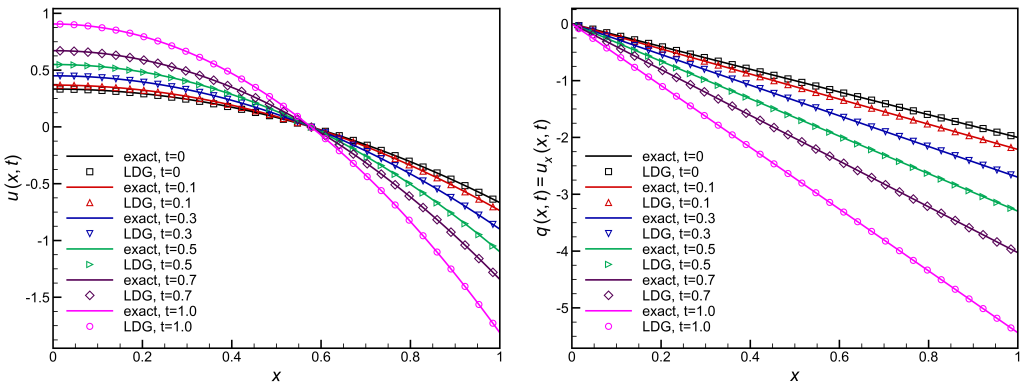


Figure 1. Example 1 ($\gamma = 1$, $a(t) = b(t) = 1 + t$; $N = 32$, $p = 3$, $\Delta t = 6.25 \times 10^{-4}$): exact (solid lines) and LDG (symbols) solution u (**left**) and auxiliary gradient $q = u_x$ (**right**) at $t = 0$, 0.1, 0.3, 0.5, 0.7, 1. The solution changes sign at $x = 1/\sqrt{3}$; $q(1,t) \neq 0$, so the zero-integral constraint does not imply a homogeneous right Neumann condition.

Figure 3 shows the convergence results at $T = 1$. For $p = 1$, both errors follow the slope h^2, so halving h reduces them by about a factor of four. For $N = 32$ and $p = 3$, the errors

follow the slope Δt^2, as expected for SDIRK2. For $p = 2, \ldots, 5$ the temporal L^2-error curves nearly coincide, because the spatial polynomial is already represented for $p \geq 2$.

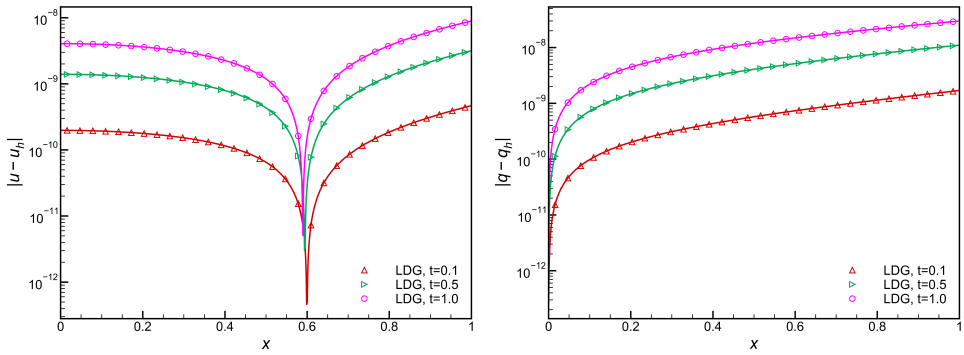


Figure 2. Example 1 ($\gamma = 1$, $a(t) = b(t) = 1 + t$; $N = 32$, $p = 3$, $\Delta t = 6.25 \times 10^{-4}$): absolute errors $|u - u_h|$ (**left**) and $|q - q_h|$ (**right**) at $t = 0.1$, 0.5, 1. The solution error has a minimum near $x = 1/\sqrt{3}$, where u vanishes; the gradient error grows toward $x = 1$.

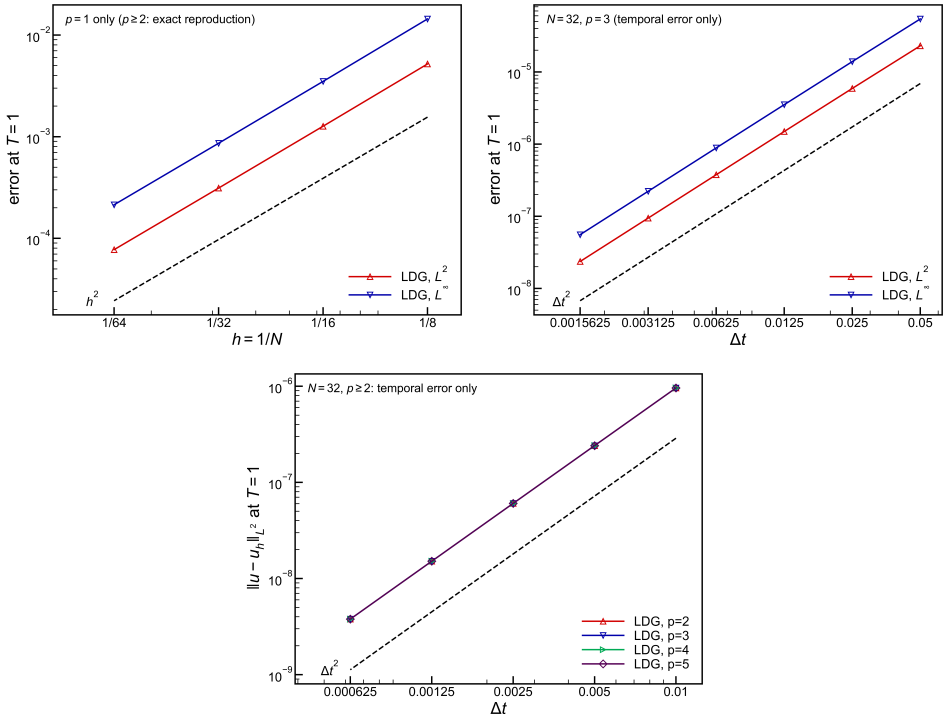


Figure 3. Example 1 ($\gamma = 1$, $a(t) = b(t) = 1 + t$), $T = 1$. **Upper left**: E_{L^2} and E_{L^∞} versus $h = 1/N$ for $p = 1$. **Upper right**: temporal convergence in both norms for $N = 32$, $p = 3$. **Lower**: temporal E_{L^2} for $N = 32$ and $p = 2, \ldots, 5$ (the curves nearly coincide because $u \in V_h^p$ for $p \geq 2$). Dashed lines: reference slopes h^2 and Δt^2.

Figure 4 and Table 3 show constraint preservation for $N = 16, 32, 64$. The stage integral residuals stay below 10^{-12} (the table gives $E_{\text{mean}} = E_{\text{stage}}$ between 3.9×10^{-14} and 4.3×10^{-13}), and the compatibility residuals are of order 10^{-15} (3.6×10^{-15} for all meshes); their small excess over the machine-precision line is consistent with accumulated floating-point and solver errors. The solution and gradient errors do not change under refinement, which is consistent with temporal-error dominance, so the small integral residuals demonstrate constraint preservation independently of the solution error, without mean correction (Section 3.8).

Table 2. Example 1 ($\gamma = 1$, $a = b = 1 + t$; $N = 32$, $p = 3$, $\Delta t = 6.25 \times 10^{-4}$): exact and LDG values of u and $q = u_x$ with absolute errors at selected points at $T = 1$. Endpoint values use interior traces. Errors are computed from unrounded values.

x	$u(x,1)$	$u_h(x,1)$	$\lvert u - u_h \rvert$	$q(x,1)$	$q_h(x,1)$	$\lvert q - q_h \rvert$
0.0	0.9060939428	0.9060939388	4.06×10^{-9}	0.00000000	0.00000000	3.77×10^{-13}
0.2	0.7973626697	0.7973626661	3.62×10^{-9}	−1.08731273	−1.08731273	4.46×10^{-9}
0.4	0.4711688503	0.4711688480	2.25×10^{-9}	−2.17462546	−2.17462545	9.30×10^{-9}
0.6	−0.0724875154	−0.0724875153	1.55×10^{-10}	−3.26193819	−3.26193818	1.49×10^{-8}
0.8	−0.8336064274	−0.8336064236	3.78×10^{-9}	−4.34925093	−4.34925090	2.16×10^{-8}
1.0	−1.8121878856	−1.8121878767	8.90×10^{-9}	−5.43656366	−5.43656363	2.99×10^{-8}

Table 3. Example 1 ($\gamma = 1$, $a = b = 1 + t$, $p = 3$, $\Delta t = 6.25 \times 10^{-4}$): errors at $T = 1$ and constraint residuals (E_{mean}, E_{stage} from Equation (69); E_{compat}, E_{balance} from Equation (70)). Since $u \in V_h^p$ for $p \geq 2$, the errors are purely temporal and identical for all meshes; they are not spatial rates. The residuals are at roundoff level; no mean correction is applied.

N	DOF	E_{L^2}	E_{L^∞}	E_{q,L^2}	E_{mean}	E_{stage}	E_{compat}	E_{balance}
16	64	3.78×10^{-9}	8.90×10^{-9}	1.55×10^{-8}	6.5×10^{-14}	6.5×10^{-14}	3.6×10^{-15}	3.6×10^{-15}
32	128	3.78×10^{-9}	8.90×10^{-9}	1.55×10^{-8}	3.9×10^{-14}	3.9×10^{-14}	3.6×10^{-15}	3.6×10^{-15}
64	256	3.78×10^{-9}	8.90×10^{-9}	1.55×10^{-8}	4.3×10^{-13}	4.3×10^{-13}	3.6×10^{-15}	3.6×10^{-15}

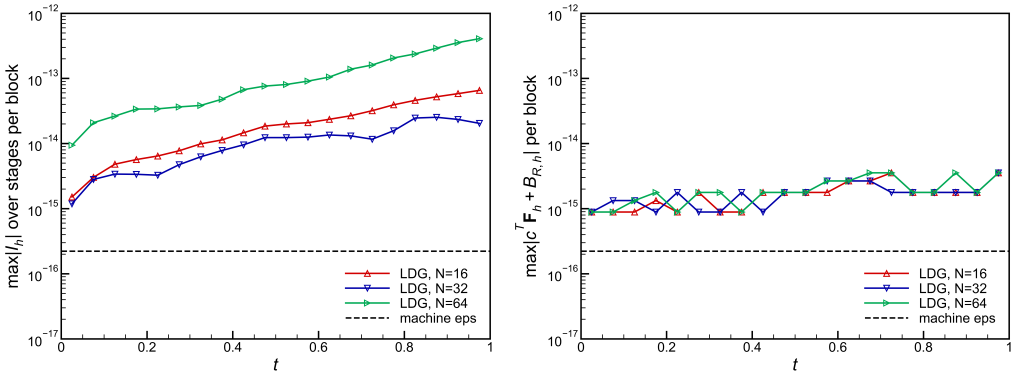


Figure 4. Example 1 ($p = 3$, $\Delta t = 6.25 \times 10^{-4}$): integral-constraint preservation for $N = 16, 32, 64$. **Left**: maximum of $|I_h^{n,i}|$ over the SDIRK2 stages within each time block. **Right**: maximum of $|F_h + z_R|$ within each time block. Dashed lines: machine precision. No mean correction is applied.

4.3. Example 2: Trigonometric Manufactured Solution

On $(x,t) \in [0,1] \times [0,1]$, consider

$$u(x,t) = e^{-t}\cos(2\pi x), \qquad u_0(x) = \cos(2\pi x). \tag{75}$$

For $b(t) = 1$ and $a(t) = -1 - 2t$, Equation (63a) yields

$$f(x,t) = e^{-t}\left[2t + 4\pi^2(1-\gamma)\right]\cos(2\pi x). \tag{76}$$

The solution satisfies $u_x(0,t) = u_x(1,t) = 0$ and has zero spatial integral, so $z_R(t) = F(t) = 0$, consistently with Lemma 1. Unlike Example 1, it is not representable in V_h^p for finite p, which allows spatial convergence studies. We consider $\gamma = 1$ and $\gamma = 0.1$. For $\gamma = 1$ the mixed-derivative and diffusion terms cancel for the exact solution, giving $f = 2te^{-t}\cos(2\pi x)$.

In this case, the semidiscrete solution is explicit. Let $\mathbf{U}_0$ be the coefficients of the initial projection, computed with the same quadrature as the load. Then $\mathbf{K} = -(\mathbf{H} + 2t\mathbf{M})$, $\mathbf{f}_h = 2te^{-t}\mathbf{M}\mathbf{U}_0$ and $F_h = 2te^{-t}I_h(0) = 0$ to roundoff, so

$$\mathbf{H}\dot{\mathbf{U}} = -(\mathbf{H} + 2t\mathbf{M})\,\mathbf{U} + 2te^{-t}\mathbf{M}\mathbf{U}_0,$$

which is solved exactly by $\mathbf{U}(t) = e^{-t}\mathbf{U}_0$ ($\mathbf{H}$ is symmetric positive definite). Hence $\|u - u_h\|(t) = e^{-t}\|u_0 - P_h u_0\|$ and $\|q - q_h\|(t) = e^{-t}\|u_0' - D_h P_h u_0\|$: for $\gamma = 1$ the spatial error is that of the initial projection, and the evolution scheme contributes only the SDIRK2 time error. We use this case to verify the projection and the time integration, and assess the spatial accuracy of the evolution scheme with $\gamma = 0.1$ and with Example 3 (Section 4.4).

Figure 5 shows that the LDG profiles follow the exact ones, capturing the trigonometric shapes and their exponential decay. The solution is symmetric about $x = 1/2$ with zero crossings at $x = 1/4$ and $x = 3/4$; the gradient $q = -2\pi e^{-t}\sin(2\pi x)$ is antisymmetric about the midpoint and vanishes at both endpoints.

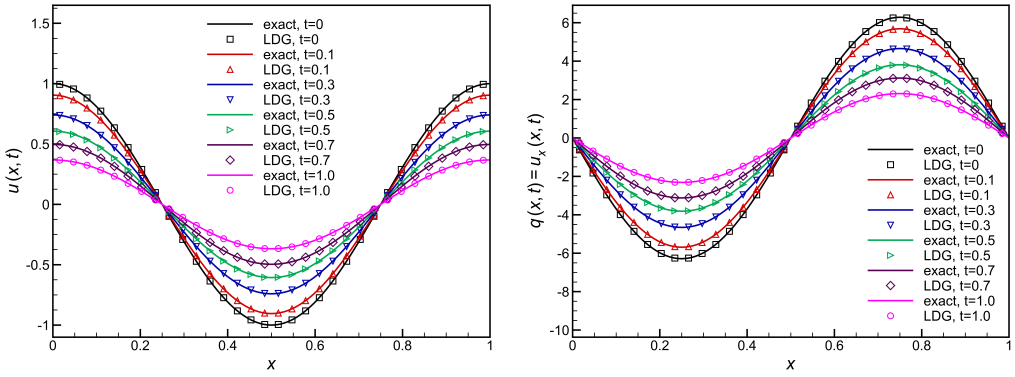


Figure 5. Example 2 ($b = 1$, $a(t) = -1 - 2t$, $\gamma = 0.1$; $N = 32$, $p = 3$, $\Delta t = 6.25 \times 10^{-4}$): exact (solid lines) and LDG (symbols) u (**left**) and $q = u_x$ (**right**) at $t = 0, 0.1, 0.3, 0.5, 0.7, 1$. The solution is symmetric about $x = 1/2$ with zeros at $x = 1/4, 3/4$; q vanishes at both endpoints.

Figure 6 shows that the gradient error exceeds the solution error, so q_h must be assessed separately from u_h. Table 4 gives pointwise results for $\gamma = 0.1$: the solution errors lie between 4.08×10^{-9} and 1.89×10^{-7}, the interior gradient errors between 4.88×10^{-8} and 1.03×10^{-6}, and the largest gradient error, 1.45×10^{-4}, occurs at $x = 0$. Although the exact gradient vanishes at both endpoints, the boundary conditions are imposed weakly through the flux, so the endpoint traces of q_h need not vanish; the larger error at $x = 0$ is consistent with the first-element effect (Remark 4).

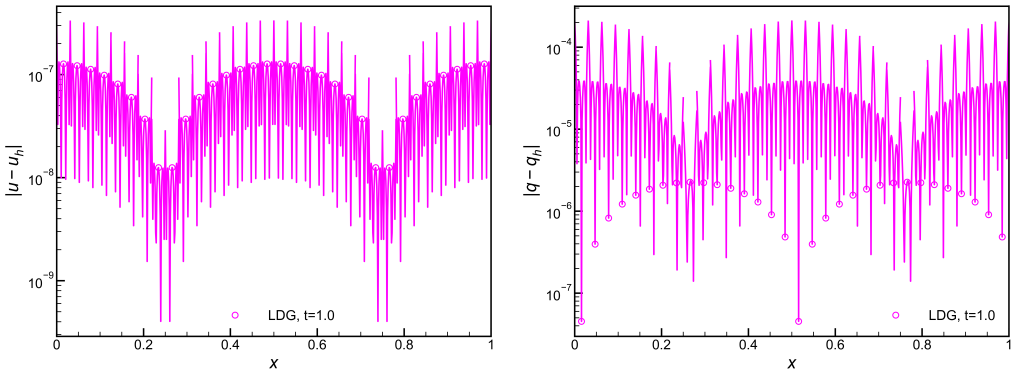


Figure 6. Example 2 ($\gamma = 0.1$, $b = 1$, $a(t) = -1 - 2t$; $N = 32$, $p = 3$, $\Delta t = 6.25 \times 10^{-4}$): absolute errors $|u - u_h|$ (**left**) and $|q - q_h|$ (**right**) at $T = 1$. The gradient error exceeds the solution error and peaks at $x = 0$ (first-element effect, Remark 4).

Figure 7 shows constraint preservation for $N = 16, 32, 64$. The completed-step residuals remain below 10^{-13}, and the stage residuals are of order 10^{-13} or smaller, with no sustained increase. The compatibility residuals stay below 7.5×10^{-17}, consistent with the vanishing exact source integral and right boundary flux. No mean correction is applied (Section 3.8).

Table 4. Example 2 ($\gamma = 0.1, b = 1, a = -1-2t; N = 32, p = 3, \Delta t = 6.25\times10^{-4}$): exact and LDG values of u and $q = u_x$ with absolute errors at selected points at $T = 1$. Endpoint values use interior traces.

x	$u(x,1)$	$u_h(x,1)$	$\lvert u-u_h\rvert$	$q(x,1)$	$q_h(x,1)$	$\lvert q-q_h\rvert$
0.0	0.3678794412	0.3678794360	5.17×10^{-9}	0.00000000	0.00014522	1.45×10^{-4}
0.2	0.1136809992	0.1136810033	4.08×10^{-9}	−2.19832405	−2.19832303	1.03×10^{-6}
0.4	−0.2976207198	−0.2976207284	8.66×10^{-9}	−1.35863898	−1.35863997	9.82×10^{-7}
0.6	−0.2976207198	−0.2976209092	1.89×10^{-7}	1.35863898	1.35863903	4.88×10^{-8}
0.8	0.1136809992	0.1136809466	5.26×10^{-8}	2.19832405	2.19832412	6.82×10^{-8}
1.0	0.3678794412	0.3678794360	5.17×10^{-9}	0.00000000	−0.00000043	4.29×10^{-7}

Table 5 complements these histories for the cancellation case $\gamma = 1$. As N doubles from 16 to 64, E_{L^2} and E_{L^∞} fall by a factor of about 16 (fourth order) and E_{q,L^2} by about 8 (third order), the approximation orders of $P_h u_0$ and $D_h P_h u_0$, as the identity above predicts. The integral residuals stay below 10^{-13} and the compatibility residual below 7.5×10^{-17}; they measure algebraic preservation, limited by roundoff and solver errors, and need not decrease with h.

Table 5. Example 2 ($\gamma = 1, p = 3, \Delta t = 1.5625\times10^{-4}$): errors and constraint residuals at $T = 1$ (Equations (69) and (70)). For $\gamma = 1$ the spatial errors are those of $P_h u_0$ and $D_h P_h u_0$ (Section 4.3). No mean correction is applied.

N	DOF	E_{L^2}	E_{L^∞}	E_{q,L^2}	E_{mean}	E_{stage}	E_{compat}	E_{balance}
16	64	1.23×10^{-6}	5.12×10^{-6}	3.69×10^{-4}	1.3×10^{-14}	1.3×10^{-14}	7.5×10^{-17}	3.5×10^{-18}
32	128	7.67×10^{-8}	3.24×10^{-7}	4.65×10^{-5}	1.1×10^{-14}	1.1×10^{-14}	5.9×10^{-17}	1.7×10^{-18}
64	256	4.80×10^{-9}	2.07×10^{-8}	5.82×10^{-6}	9.5×10^{-14}	9.5×10^{-14}	5.6×10^{-17}	8.7×10^{-19}

Table 6 reports the spatial refinement study for $\gamma = 0.1$, where the cancellation is absent, so the errors are not fixed by the initial projection and the table assesses the spatial accuracy of the evolution scheme. Starting from $\Delta t = 0.01$, the time step is halved until Equation (67) holds; the accepted values range from 2.5×10^{-3} down to 1.95×10^{-5} ($p = 4$, $N = 64$). The finest-mesh L^2 rates of u_h are 2.02, 3.00, 4.00 and 4.99 for $p = 1, \dots, 4$, i.e., order $p+1$. The auxiliary-gradient rates depend on the parity of p, as in Example 3. For odd p they approach $p + \frac{1}{2}$ (1.50 for $p = 1$, 3.50 for $p = 3$), consistently with the lower bound on the first element (Remark 4). For even p they exceed $p+1$ (about 3.2 for $p = 2$ and 5.3 for $p = 4$), because the exact solution is even about $x = 0$ and the leading term of that bound vanishes. These even-p rates are observations for this solution and do not establish a general superconvergence result.

Table 6. Example 2 ($\gamma = 0.1, b = 1, a = -1-2t$): spatial convergence at $T = 1$ for $p = 1, \dots, 4$: E_{L^2} and E_{q,L^2} with rates r_h (Equation (66)). Δt (last column) is chosen by Equation (67) so that the estimated temporal error is at most 10% of each error.

p	N	DOF	E_{L^2}	Rate	E_{q,L^2}	Rate	Δt
1	8	16	1.06×10^{-2}	–	1.79×10^{-1}	–	2.50×10^{-3}
1	16	32	2.59×10^{-3}	2.03	6.58×10^{-2}	1.44	2.50×10^{-3}
1	32	64	6.32×10^{-4}	2.04	2.33×10^{-2}	1.50	2.50×10^{-3}
1	64	128	1.55×10^{-4}	2.02	8.23×10^{-3}	1.50	2.50×10^{-3}
2	8	24	6.14×10^{-4}	–	7.96×10^{-3}	–	2.50×10^{-3}
2	16	48	7.68×10^{-5}	3.00	7.96×10^{-4}	3.32	2.50×10^{-3}
2	32	96	9.60×10^{-6}	3.00	8.26×10^{-5}	3.27	2.50×10^{-3}
2	64	192	1.20×10^{-6}	3.00	9.05×10^{-6}	3.19	2.50×10^{-3}

Table 6. *Cont.*

p	N	DOF	E_{L^2}	Rate	E_{q,L^2}	Rate	Δt
3	8	32	3.01×10^{-5}	–	1.16×10^{-3}	–	2.50×10^{-3}
3	16	64	1.88×10^{-6}	4.00	1.08×10^{-4}	3.41	2.50×10^{-3}
3	32	128	1.17×10^{-7}	4.01	9.72×10^{-6}	3.48	6.25×10^{-4}
3	64	256	7.28×10^{-9}	4.00	8.61×10^{-7}	3.50	1.56×10^{-4}
4	8	40	1.15×10^{-6}	–	2.44×10^{-5}	–	2.50×10^{-3}
4	16	80	3.62×10^{-8}	4.99	5.75×10^{-7}	5.41	6.25×10^{-4}
4	32	160	1.13×10^{-9}	5.00	1.37×10^{-8}	5.39	7.81×10^{-5}
4	64	320	3.54×10^{-11}	4.99	3.42×10^{-10}	5.32	1.95×10^{-5}

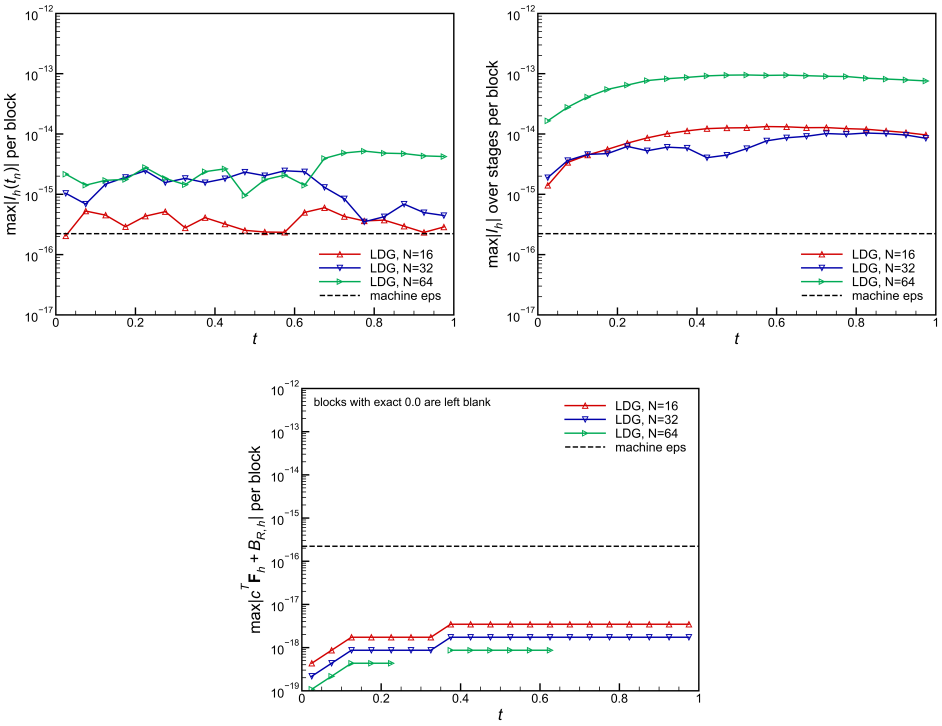


Figure 7. Example 2 ($\gamma = 1$, $p = 3$, $\Delta t = 1.5625 \times 10^{-4}$): integral-constraint preservation for $N = 16, 32, 64$. **Upper left**: maximum of $|I_h^n|$ at completed steps. **Upper right**: maximum of $|I_h^{n,i}|$ over stages. **Lower**: maximum of $|F_h + z_R|$ (exactly zero values are omitted from the logarithmic plot). Each value is a maximum within a time block; dashed lines: machine precision.

4.4. Example 3: Mixed Trigonometric–Polynomial Manufactured Solution

The final benchmark combines two trigonometric modes and a polynomial component with distinct temporal behaviors. On $(x,t) \in [0,1] \times [0,1]$, consider

$$\begin{aligned} u(x,t) &= e^{-t}\cos(2\pi x) + \frac{1}{4}e^{-2t}\cos(4\pi x) + \frac{1}{10}\sin t\left(x^2 - \frac{1}{3}\right), \\ u_0(x) &= \cos(2\pi x) + \frac{1}{4}\cos(4\pi x). \end{aligned} \tag{77}$$

For $\gamma = 0.1$, $b(t) = 1 + t$ and $a(t) = -1$, Equation (63a) yields

$$\begin{aligned} f(x,t) = {} & 4\pi^2[b(t) - \gamma]e^{-t}\cos(2\pi x) + \frac{1}{4}\left[-1 + 16\pi^2(b(t) - 2\gamma)\right]e^{-2t}\cos(4\pi x) \\ & + \frac{1}{10}(\cos t + \sin t)\left(x^2 - \frac{1}{3}\right) - \frac{\gamma}{5}\cos t - \frac{b(t)}{5}\sin t. \end{aligned} \tag{78}$$

The solution satisfies $u_x(0,t) = 0$ and $\int_0^1 u\,dx = 0$. Its right derivative and combined boundary flux are

$$u_x(1,t) = \frac{1}{5}\sin t, \qquad z_R(t) = \gamma u_{xt}(1,t) + b(t)u_x(1,t) = \frac{\gamma}{5}\cos t + \frac{b(t)}{5}\sin t, \tag{79}$$

and the integrated source is

$$F(t) = \int_0^1 f(x,t)\,dx = -\frac{\gamma}{5}\cos t - \frac{b(t)}{5}\sin t. \tag{80}$$

Hence, $z_R(t) + F(t) = 0$, consistently with Lemma 1. This benchmark combines non-polynomial spatial structure with a time-dependent, nonzero right boundary flux, and therefore tests spatial and temporal accuracy, auxiliary-gradient approximation and integral-constraint preservation beyond the polynomial reproduction and spatial-term cancellation cases of Examples 1 and 2.

Figure 8 shows that the LDG profiles follow the exact ones, capturing the shape produced by the two decaying trigonometric modes and the polynomial component. The endpoint values of u differ because of the term $\frac{1}{10}\sin t\,(x^2 - \frac{1}{3})$. The gradient satisfies $q(0,t) = 0$ and $q(1,t) = \frac{1}{5}\sin t \neq 0$ for $t > 0$, so the evolving right boundary derivative is reproduced.

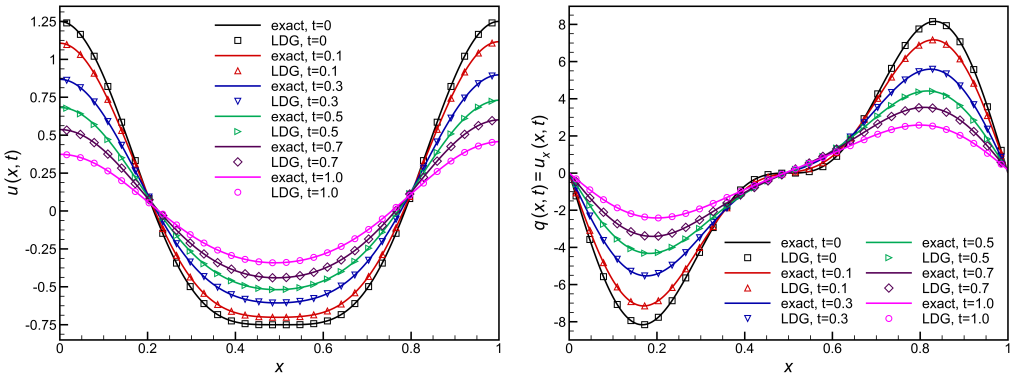


Figure 8. Example 3 ($\gamma = 0.1$, $b(t) = 1 + t$, $a(t) = -1$; $N = 32$, $p = 3$, $\Delta t = 1.25 \times 10^{-3}$): exact (solid lines) and LDG (symbols) u (**left**) and $q = u_x$ (**right**) at $t = 0$, 0.1, 0.3, 0.5, 0.7, 1. The right derivative $q(1,t) = \frac{1}{5}\sin t$ is nonzero for $t > 0$.

Figure 9 shows that the gradient error is generally larger than the solution error, with a pronounced peak near the left boundary. Table 7 gives pointwise values: the solution errors lie between 7.31×10^{-9} and 1.49×10^{-7}, the interior gradient errors between 3.09×10^{-8} and 3.51×10^{-6}, and the largest gradient error, 3.56×10^{-4}, occurs at $x = 0$. This nonzero endpoint error is compatible with the weak imposition of the boundary condition through the numerical flux; the trace $q_h(0^+,t)$ is not constrained separately. At $x = 1$, the computed gradient approximates the nonzero exact value $q(1,1) = \frac{1}{5}\sin 1$ with an error of 2.74×10^{-6}.

Table 7. Example 3 ($\gamma = 0.1$, $b = 1 + t$, $a = -1$; $N = 32$, $p = 3$, $\Delta t = 1.25 \times 10^{-3}$): exact and LDG values of u and $q = u_x$ with absolute errors at selected points at $T = 1$. Endpoint values use interior traces.

x	$u(x,1)$	$u_h(x,1)$	$\lvert u - u_h\rvert$	$q(x,1)$	$q_h(x,1)$	$\lvert q - q_h\rvert$
0.0	0.3736642292	0.3736642015	2.76×10^{-8}	0.00000000	0.00035625	3.56×10^{-4}
0.2	0.0616257143	0.0616257022	1.21×10^{-8}	−2.41457289	−2.41456995	2.94×10^{-6}
0.4	−0.3017509912	−0.3017509839	7.31×10^{-9}	−0.88696219	−0.88695868	3.51×10^{-6}
0.6	−0.2849215715	−0.2849216783	1.07×10^{-7}	1.05525639	1.05525619	2.00×10^{-7}
0.8	0.1121139734	0.1121141225	1.49×10^{-7}	2.58286709	2.58286712	3.09×10^{-8}
1.0	0.4578113276	0.4578113036	2.40×10^{-8}	0.16829420	0.16829146	2.74×10^{-6}

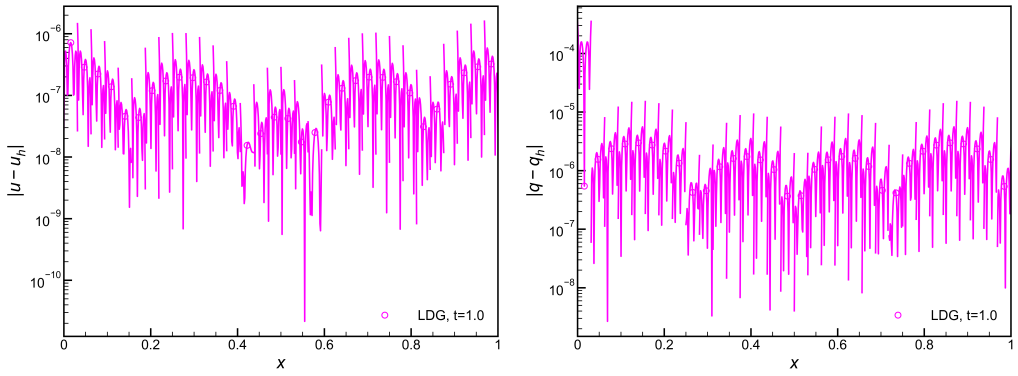


Figure 9. Example 3 ($N = 32$, $p = 3$, $\Delta t = 1.25 \times 10^{-3}$): absolute errors $|u - u_h|$ (**left**) and $|q - q_h|$ (**right**) at $T = 1$. The gradient error is larger than the solution error and peaks near the left boundary.

Figure 10 and Table 8 show the spatial convergence at $T = 1$. The solution L^2-errors follow h^{p+1}: the finest-mesh rates are approximately 2.04, 3.00, 4.01 and 5.00, and the L^∞-rates also approach $p + 1$. Since the estimated temporal errors are below 10% of the reported errors, these results are numerical evidence of optimal-order spatial convergence for the solution.

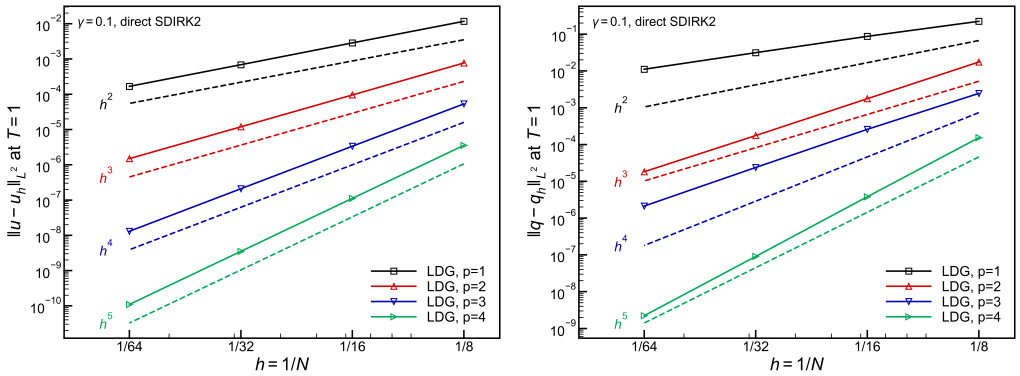


Figure 10. Example 3, $T = 1$: E_{L^2} for u (**left**) and E_{q,L^2} for q (**right**) versus $h = 1/N$ for $p = 1, \ldots, 4$, with Δt chosen by Equation (67) (Table 8). Dashed lines: h^{p+1}; for q, they are for reference only, since the full-domain rates are $p + \frac{1}{2}$ for odd p (Table 9).

The full-domain gradient rates depend on the parity of p: they approach 1.5 and 3.5 for $p = 1, 3$ and exceed $p + 1$ for $p = 2, 4$, whereas the interior error E_q^{int} approaches $p + 1$ for all tested degrees. Table 9 separates the contributions of the first element, the interior and the last element.

Left boundary element. On K_1 both interface traces $\hat{u}_h$ come from K_1, so $q_h|_{K_1} = \partial_x u_h \in \mathbb{P}^{p-1}(K_1)$. Hence, for any u_h, any γ and any initialization, $\|q - q_h\|_{K_1} \geq \text{dist}(q, \mathbb{P}^{p-1}) \propto h^{p+1/2} |u^{(p+1)}(0, t)|$ (Remark 4). In every row of Table 9, this bound reproduces the measured K_1 error to four digits, so $q_h|_{K_1}$ is, to that accuracy, the best $\mathbb{P}^{p-1}$ approximation of q, and the localized error near the left boundary in Figure 9 is a property of the closure and not of the time integrator. The rates on K_1 are $p + \frac{1}{2}$ for odd p (1.49 and 3.48 at $N = 64$) and $p + \frac{3}{2}$ for even p (3.49 and 5.49), because u is even about $x = 0$ and $u^{(p+1)}(0, t) = 0$ for even p. Without this symmetry, the leading boundary coefficient need not vanish for even p, so the same parity pattern is not expected in general.

Table 8. Example 3 ($\gamma = 0.1$, $b = 1 + t$, $a = -1$): spatial convergence at $T = 1$ for $p = 1, \ldots, 4$: E_{L^2}, E_{L^∞}, E_{q,L^2} and E_q^{int} (without the two boundary elements) with rates r_h. Δt is chosen by Equation (67) so that the estimated temporal error is at most 10% of each error.

p	N	DOF	E_{L^2}	Rate	E_{L^∞}	Rate	E_{q,L^2}	Rate	E_q^{int}	Rate
1	8	16	1.17×10^{-2}	–	4.11×10^{-2}	–	2.24×10^{-1}	–	6.39×10^{-2}	–
1	16	32	2.86×10^{-3}	2.03	1.23×10^{-2}	1.74	8.72×10^{-2}	1.36	1.86×10^{-2}	1.78
1	32	64	6.88×10^{-4}	2.06	3.20×10^{-3}	1.95	3.14×10^{-2}	1.47	4.74×10^{-3}	1.97
1	64	128	1.68×10^{-4}	2.04	8.04×10^{-4}	1.99	1.11×10^{-2}	1.50	1.19×10^{-3}	2.00
2	8	24	7.70×10^{-4}	–	4.30×10^{-3}	–	1.75×10^{-2}	–	4.17×10^{-3}	–
2	16	48	9.54×10^{-5}	3.01	5.56×10^{-4}	2.95	1.76×10^{-3}	3.31	6.43×10^{-4}	2.70
2	32	96	1.19×10^{-5}	3.00	6.95×10^{-5}	3.00	1.75×10^{-4}	3.33	9.38×10^{-5}	2.78
2	64	192	1.49×10^{-6}	3.00	8.77×10^{-6}	2.99	1.82×10^{-5}	3.27	1.26×10^{-5}	2.90
3	8	32	5.33×10^{-5}	–	2.96×10^{-4}	–	2.46×10^{-3}	–	4.68×10^{-4}	–
3	16	64	3.36×10^{-6}	3.99	2.39×10^{-5}	3.63	2.59×10^{-4}	3.25	3.52×10^{-5}	3.73
3	32	128	2.09×10^{-7}	4.01	1.60×10^{-6}	3.90	2.38×10^{-5}	3.44	2.26×10^{-6}	3.96
3	64	256	1.30×10^{-8}	4.01	1.02×10^{-7}	3.98	2.13×10^{-6}	3.49	1.42×10^{-7}	3.99
4	8	40	3.56×10^{-6}	–	2.25×10^{-5}	–	1.54×10^{-4}	–	3.38×10^{-5}	–
4	16	80	1.12×10^{-7}	4.99	8.13×10^{-7}	4.79	3.81×10^{-6}	5.33	1.14×10^{-6}	4.89
4	32	160	3.51×10^{-9}	4.99	2.62×10^{-8}	4.96	9.08×10^{-8}	5.39	3.88×10^{-8}	4.87
4	64	320	1.10×10^{-10}	5.00	8.17×10^{-10}	5.00	2.22×10^{-9}	5.35	1.27×10^{-9}	4.94

Table 9. Example 3: auxiliary-gradient L^2-errors on the left element K_1, in the interior (without the two boundary elements) and on the right element K_N at $T = 1$, with rates. The last column is $\mathrm{dist}(q, \mathbb{P}^{p-1})_{K_1}$ divided by the measured K_1 error; it is at most 1 by definition and equals 1.0000 in every row.

p	N	$E_q^{K_1}$	Rate	E_q^{int}	Rate	$E_q^{K_N}$	Rate	Bound/$E_q^{K_1}$
1	8	2.12×10^{-1}	–	6.39×10^{-2}	–	2.97×10^{-2}	–	1.0000
1	16	8.52×10^{-2}	1.32	1.86×10^{-2}	1.78	2.89×10^{-3}	3.36	1.0000
1	32	3.11×10^{-2}	1.45	4.74×10^{-3}	1.97	2.62×10^{-4}	3.47	1.0000
1	64	1.11×10^{-2}	1.49	1.19×10^{-3}	2.00	2.33×10^{-5}	3.49	1.0000
2	8	1.66×10^{-2}	–	4.17×10^{-3}	–	3.55×10^{-3}	–	1.0000
2	16	1.59×10^{-3}	3.39	6.43×10^{-4}	2.70	3.93×10^{-4}	3.18	1.0000
2	32	1.44×10^{-4}	3.47	9.38×10^{-5}	2.78	3.67×10^{-5}	3.42	1.0000
2	64	1.27×10^{-5}	3.49	1.26×10^{-5}	2.90	3.28×10^{-6}	3.48	1.0000
3	8	2.40×10^{-3}	–	4.68×10^{-4}	–	2.35×10^{-4}	–	1.0000
3	16	2.56×10^{-4}	3.23	3.52×10^{-5}	3.73	5.75×10^{-6}	5.36	1.0000
3	32	2.37×10^{-5}	3.43	2.26×10^{-6}	3.96	1.30×10^{-7}	5.46	1.0000
3	64	2.12×10^{-6}	3.48	1.42×10^{-7}	3.99	2.90×10^{-9}	5.49	1.0000
4	8	1.49×10^{-4}	–	3.38×10^{-5}	–	1.75×10^{-5}	–	1.0000
4	16	3.60×10^{-6}	5.37	1.14×10^{-6}	4.89	5.08×10^{-7}	5.10	1.0000
4	32	8.13×10^{-8}	5.47	3.88×10^{-8}	4.87	1.20×10^{-8}	5.41	1.0000
4	64	1.81×10^{-9}	5.49	1.27×10^{-9}	4.94	2.68×10^{-10}	5.48	1.0000

Right element and interior. On K_N and in the interior, q_h agrees with the Gauss–Radau projection P^+q of the exact gradient to within 0.45% of the error on K_N. The error on K_N scales as $h^{p+3/2}$, and one order faster where $\partial_x^{p+2}u(1) = 0$, which gives the alternating rates 3.5, 3.5, 5.5, 5.5 for $p = 1, \ldots, 4$. The interior errors approach rate $p + 1$ for all tested degrees. Together with the first-element bound, this shows that boundary-element errors reduce the full-domain gradient rate for odd p.

Initial gradient. The initialization $q_h(0) = D_h P_h u_0$ can introduce an $O(h^p)$ gradient error. Equation (58) shows that the high-frequency modal decay rates approach $b(t)/\gamma$, rather than increasing without bound under mesh refinement. The corresponding damping factor is therefore approximately $\exp(-\int_0^t b(s)/\gamma \, \mathrm{d}s)$. In Example 3, $\int_0^1 b(t)/\gamma \, \mathrm{d}t = 15$, so strong damping of the initial high-frequency components is consistent with the rates observed in

Table 8. In contrast, the cancellation case $\gamma = 1$ retains the initial-projection gradient rate of approximately p (Table 5). These observations explain the behavior on the tested meshes but do not establish the asymptotic gradient rate for arbitrary initialization.

The reduced full-domain rates for odd p are thus a consequence of the weak (flux-based) boundary closure. For periodic data, every interface trace is collocated by the Gauss–Radau projections and this term is absent [24,25]. Parity-dependent rates, including a half-order loss for odd degrees, have been reported for LDG with generalized alternating fluxes [31], and the dependence of superconvergence on the choice of fluxes is analyzed in [37]. The higher rates for even p are observations at $T = 1$ on uniform meshes for this solution and not a general superconvergence result.

Figure 11 shows that the completed-step and stage integral residuals stay below 10^{-13} with similar temporal patterns and no sustained drift. Table 10 gives the values for $p = 3$: $E_{\text{mean}} = E_{\text{stage}}$ lie between 9.6×10^{-15} and 3.8×10^{-14}, E_{compat} between 5.8×10^{-15} and 7.2×10^{-15}, and E_{balance} between 1.1×10^{-16} and 8.9×10^{-16}. All are at roundoff level, so the zero-integral constraint is preserved without mean correction for the time-dependent, nonzero right boundary flux, while mesh refinement reduces the L^2-errors of u and q from 3.36×10^{-6} to 1.30×10^{-8} and from 2.59×10^{-4} to 2.13×10^{-6}.

Table 10. Example 3 ($p = 3$, $\Delta t = 3.125\times10^{-4}$): L^2-errors of u and q at $T = 1$ and constraint residuals E_{mean}, E_{stage}, E_{compat}, E_{balance} (Equations (69)–(70)). No mean correction is applied.

N	DOF	E_{L^2}	E_{q,L^2}	E_{mean}	E_{stage}	E_{compat}	E_{balance}
16	64	3.36×10^{-6}	2.59×10^{-4}	9.6×10^{-15}	9.6×10^{-15}	7.2×10^{-15}	8.9×10^{-16}
32	128	2.09×10^{-7}	2.38×10^{-5}	2.0×10^{-14}	2.0×10^{-14}	6.3×10^{-15}	2.3×10^{-16}
64	256	1.30×10^{-8}	2.13×10^{-6}	3.8×10^{-14}	3.8×10^{-14}	5.8×10^{-15}	1.1×10^{-16}

Table 11 shows that constraint preservation does not depend on the accuracy of the source quadrature (Remark 1). With the same m-point rule in the volume load and in F_h, the discrete mean stays at roundoff level for every m, and only the accuracy deteriorates, for $m = 2$ and $m = 1$ (rates 3.00 and 1.99 instead of 4.00). If F_h is assembled with a different rule, the mean drifts by the quadrature defect (2.7×10^{-5} for $N = 16$, $m = 1$) with no change in E_{L^2}.

Table 11. Quadrature sensitivity, Example 3 ($p = 3$, $\Delta t = 3.125\times10^{-4}$); m is the number of Gauss points per element. (**a**) The same m-point rule in the volume load and in F_h: the mean is preserved for every m and only the accuracy depends on m (E_{mean}: maximum over $N = 16, 32, 64$; E_{L^2} and the rate: $N = 64$ and $N = 32 \to 64$). (**b**) The load uses m points and F_h uses 12: the mean drifts by the quadrature defect while E_{L^2} is unchanged. "Roundoff": below 5×10^{-14}.

(a) Same Rule in Load and F_h				
m	$\max E_{\text{mean}}$	E_{compat} ($N = 16 \to 64$)	E_{L^2}	Rate
1	4.7×10^{-14}	$4.6\times10^{-5} \to 2.9\times10^{-6}$	7.26×10^{-5}	1.99
2	3.3×10^{-14}	roundoff	1.57×10^{-6}	3.00
≥3	$\leq 4.4\times10^{-14}$	roundoff	1.30×10^{-8}	4.00
(b) Load with m Points, F_h with 12 Points				
m	E_{mean} ($N = 16$)	E_{mean} ($N = 64$)	E_{L^2}	
1	2.7×10^{-5}	1.7×10^{-6}	as in (a)	
≥2	roundoff	roundoff	as in (a)	

Table 12 compares the exact and discrete energies. Both decrease from approximately 1.4993 at $t = 0$ to 0.18136 at $t = 1$, and the relative difference stays below 1.4×10^{-7} in absolute value; after the initial time it is negative, a slight underestimation. Since this example has a nonzero source and boundary flux, the observed decrease is specific to the prescribed data and is not a general energy-decay result for forced problems.

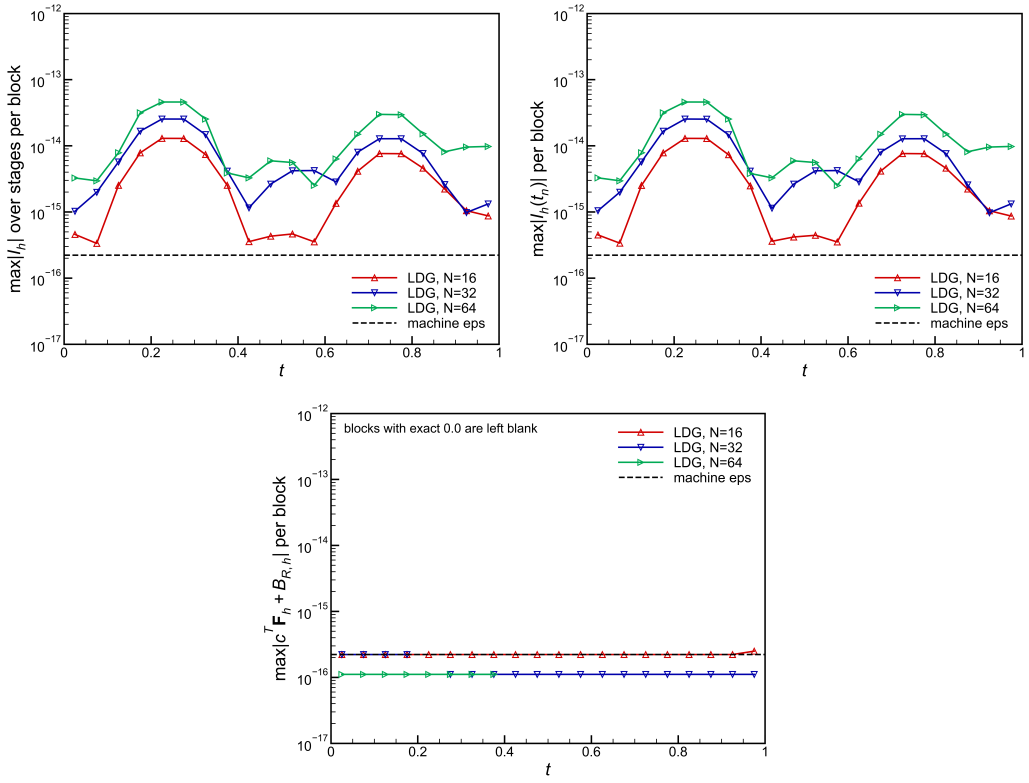


Figure 11. Example 3 ($p = 3$, $\Delta t = 3.125 \times 10^{-4}$): integral-constraint preservation for $N = 16, 32, 64$. **Upper left**: maximum of $|I_h^n|$ at completed steps. **Upper right**: maximum of $|I_h^{n,i}|$ over stages. **Lower**: maximum of E_{compat} and E_{balance}. Each value is a maximum within a time block; dashed lines: machine precision.

Table 12. Example 3 ($\gamma = 0.1$, $b = 1 + t$, $a = -1$; $N = 32$, $p = 3$, $\Delta t = 1.25 \times 10^{-3}$): exact energy $\mathcal{E}(t)$ and discrete energy $\mathcal{E}_h(t)$ (Equations (43) and (44)) at selected times, and the signed relative difference $(\mathcal{E}_h - \mathcal{E})/\mathcal{E}$.

t	$\mathcal{E}$	$\mathcal{E}_h$	$(\mathcal{E}_h - \mathcal{E})/\mathcal{E}$
0.0	1.4993255501	1.4993255636	8.98×10^{-9}
0.1	1.1913160756	1.1913159653	-9.26×10^{-8}
0.2	0.9518766658	0.9518765431	-1.29×10^{-7}
0.3	0.7643280792	0.7643279741	-1.38×10^{-7}
0.4	0.6164146558	0.6164145722	-1.36×10^{-7}
0.5	0.4990415239	0.4990414587	-1.31×10^{-7}
0.6	0.4053925093	0.4053924586	-1.25×10^{-7}
0.7	0.3303097269	0.3303096873	-1.20×10^{-7}
0.8	0.2698538943	0.2698538631	-1.15×10^{-7}
0.9	0.2209901315	0.2209901069	-1.11×10^{-7}
1.0	0.1813614320	0.1813614125	-1.08×10^{-7}

4.5. Comparison with UHPB–CN and Computational Cost

The LDG scheme has $N_{\text{dof}} = N(p + 1)$ unknowns and is solved as described in Section 4.1. Timings are medians of five single-threaded runs on the machine; they are meaningful to an order of magnitude only. As a benchmark we reimplemented the UHPB–CN scheme of [15] in the same environment, with an $O(M)$ tridiagonal-plus-Schur stepper (its best case). On Example 1, it reproduces the published nodal errors of [15] to three digits (Table 13), except for the $M = 800$ entries, which differ by about 1% and are sensitive to roundoff in the hyperbolic functions. This is a comparison with our reimplementation, not with the authors' code.

In Table 13, the LDG error for $p = 2$ is purely temporal, because the quadratic solution is reproduced in space; it is independent of N and equals $C\Delta t^2$, so the comparison measures the time-stepping error at equal Δt. LDG is more accurate than UHPB–CN for $M \leq 400$. At $\Delta t = 0.0025$ it saturates at 1.42×10^{-7}, the SDIRK2 temporal error, and at $M = 800$ UHPB–CN is slightly more accurate.

Table 13. Example 1 at $t = 1$: UHPB–CN (our reimplementation), the published UHPB–CN values of [15], and LDG with $p = 2$ ($N = 32$). UHPB–CN errors are nodal discrete norms; LDG errors are the norms of Equation (65). (**a**) L^2 error with $\Delta t = \Delta\xi$; (**b**) L^∞ error with $\Delta t = 0.0025$. The LDG error is purely temporal and independent of N.

M	UHPB–CN (Ours)	UHPB–CN (Published)	LDG $p = 2$
(a) L^2 error, $\Delta t = \Delta\xi$			
5	1.93×10^{-3}	1.93×10^{-3}	4.18×10^{-4}
10	4.24×10^{-4}	4.24×10^{-4}	1.02×10^{-4}
40	2.37×10^{-5}	2.38×10^{-5}	6.16×10^{-6}
(b) L^∞ error, $\Delta t = 0.0025$			
10	1.38×10^{-3}	1.38×10^{-3}	1.42×10^{-7}
40	8.61×10^{-5}	8.61×10^{-5}	1.42×10^{-7}
80	2.13×10^{-5}	2.13×10^{-5}	1.42×10^{-7}
400	5.21×10^{-7}	5.21×10^{-7}	1.42×10^{-7}
800	1.28×10^{-7}	1.27×10^{-7}	1.42×10^{-7}

Table 14 gives the smallest mesh meeting each L^2 target for $\Delta t = T/n_{\text{steps}}$, accepted by the step-doubling test (67). Relative to the fastest LDG degree, UHPB–CN is faster at every target: by 11–25× at 10^{-4} and 10^{-6}, and by 3.2× (Example 2) and 6.3× (Example 3) at 10^{-8}, where it reaches the target only at the roundoff limit. LDG with $p \geq 2$ needs far fewer unknowns: at 10^{-8}, $p = 4$ uses 105 and 130 DOF against 9261 and 9833, about 76–88 times fewer. LDG with $p = 1$ is the slowest (107–121 s).

Table 14. Time to accuracy: DOF / wall time [s] to reach the L^2 target with $\Delta t = T/n_{\text{steps}}$ ($n_{\text{steps}} = 400$ for 10^{-4} and 10^{-6}; 3200 for 10^{-8}, except UHPB–CN on Example 3 with 1600). UHPB–CN: nodal discrete L^2 norm; LDG: continuous L^2 norm. † Roundoff-limited: the error criterion is met, but the order test fails at roundoff level.

	Target	UHPB–CN	LDG $p = 1$	LDG $p = 2$	LDG $p = 3$	LDG $p = 4$
Ex. 2 ($\gamma = 0.1$)	10^{-4}	93/0.035	160/1.11	45/0.97	24/0.86	20/0.92
	10^{-6}	927/0.050	1590/2.52	207/1.09	76/0.93	45/0.92
	10^{-8}	9261 †/2.24	15,930/107	951/12.6	240/8.11	105/7.06
Ex. 3	10^{-4}	99/0.046	166/0.88	48/0.81	28/0.82	25/0.80
	10^{-6}	985/0.075	1644/1.93	222/0.97	88/0.87	55/0.84
	10^{-8}	9833 †/1.36	16,460/121	1026/13.6	276/9.28	130/8.61

Table 15 shows that UHPB–CN costs 0.13–0.60 ms per step, against 2.5–21.7 ms for LDG-SDIRK2. Between 39% and 70% of an SDIRK2 step is spent outside the factorizations and solves, mostly assembling the stage matrices in Python, so part of the gap reflects the implementation. Because the stiffness of the semidiscrete system is bounded by b/γ (Remark 2), explicit RK4 with a single factorization of $\mathbf{H}$ is stable for $\Delta t \leq 2.785\,\gamma/b$ (when $b/\gamma \geq |a|$; verified to within 7×10^{-4} for $p = 1, 3, 4$ and $\gamma = 0.01, 0.1, 1$) and costs 1.4–8.1 ms per step; SDIRK2 has no such restriction, which matters for small γ or large Δt. A general sparse LU on the UHPB–CN arrow matrix is far slower (734 ms per step at 6401 DOF), because the dense Simpson row of [15] fills in the factors.

Table 15. Wall time per step [ms] on Example 3 ($\Delta t = 0.005$, 200 steps, medians of five runs). DOF = $M + 1$ for UHPB–CN and $N(p + 1)$ for LDG.

	DOF			
Scheme	**101**	**401**	**1601**	**6401**
UHPB–CN, $O(M)$ solver	0.13	0.15	0.23	0.60
UHPB–CN, general sparse LU	1.8	6.5	51	734
LDG-SDIRK2, $p = 1$	3.7	2.6	4.7	14.8
LDG-SDIRK2, $p = 4$	2.5	2.9	6.0	21.7
LDG-RK4, $p = 1$	1.4	1.6	2.8	8.1
LDG-RK4, $p = 4$	1.4	1.5	2.4	6.6

5. Conclusions and Outlook

A modal LDG scheme has been developed for one-dimensional third-order pseudo-parabolic problems with a homogeneous left Neumann condition and a zero-integral constraint, imposed through a compatible right boundary flux. Consistent source quadrature yields the discrete law $I_h' = a(t)I_h$; hence, with compatible initial data and uniquely solvable stage systems (Lemma 2), any Runge–Kutta method preserves the zero integral at every stage and step without mean correction (Proposition 1). We use SDIRK2 for its L-stability and second-order accuracy. The analysis also gives an energy-norm estimate of order $h^{p+1/2}$ for Radau-projected initial data (Theorem 1). The L^2-projected initialization used in the experiments introduces an additional $O(h^{p+1} + \sqrt{\gamma}h^p)$ contribution. The estimate is uniform for $0 < \gamma \le \gamma_{\max}$ under uniform coefficient bounds and solution regularity.

Three manufactured-solution benchmarks show solution convergence of approximately order $p + 1$ in space and second order in time, integral residuals below 10^{-12}, and a discrete energy within 1.4×10^{-7} (relative) of the exact one. The gradient converges at order $p + 1$ in the interior, but the first element limits its full-domain rate to $p + \frac{1}{2}$ for odd p (Remark 4); the higher rates for even p are specific to the even solutions tested. Against UHPB–CN, LDG with $p = 4$ needs 76–88 times fewer unknowns for an L^2 error of 10^{-8}, but UHPB–CN is faster in wall time by a factor of about 3 to 25 in our implementation (Section 4.5).

Open questions are an optimal-order L^2 estimate for u_h in the constrained setting and a sharp analysis of the interior gradient error. Further developments include nonzero prescribed integrals, nonlinear models, and extensions to higher dimensions; spatially varying diffusion $b(x, t)$, which requires a stability analysis for non-commuting mass and diffusion matrices, and the non-conservative form, which requires a nonlocal correction of the right numerical flux (Remark 6); adaptive mesh and polynomial-degree refinement; and structured block solvers with optimized assembly to narrow the cost gap to spline schemes.

Author Contributions: Conceptualization, S.S.; Methodology, S.S.; Software, S.S.; Validation, S.S.; Formal Analysis, N.A.A. and A.H.M.; Investigation, N.A.A. and C.P.; Data Curation, C.P.; Writing—Original Draft, N.A.A., C.P. and S.S.; Writing—Review & Editing, A.H.M.; Visualization, C.P. and A.H.M. All authors have read and agreed to the published version of the manuscript.

Funding: There is no funding for this research work.

Data Availability Statement: The original contributions presented in this study are included in the article. Further inquiries can be directed to the corresponding author.

Conflicts of Interest: The authors declare no conflicts of interest.

References

1. Showalter , R.E.; Ting, T.W. Pseudoparabolic partial differential equations. *SIAM J. Math. Anal.* **1970**, *1*, 1–26. [CrossRef]
2. Barenblatt, G.I.; Zheltov, I.P.; Kochina, I.N. Basic concepts in the theory of seepage of homogeneous liquids in fissured rocks. *J. Appl. Math. Mech.* **1960**, *24*, 1286–1303. [CrossRef]

3. Chen, P.J.; Gurtin, M.E. On a theory of heat conduction involving two temperatures. *Z. Angew. Math. Phys.* **1968**, *19*, 614–627. [CrossRef]
4. Ting, T.W. A cooling process according to two-temperature theory of heat conduction. *J. Math. Anal. Appl.* **1974**, *45*, 23–31. [CrossRef]
5. Benjamin, T.B.; Bona, J.L.; Mahony, J.J. Model equations for long waves in nonlinear dispersive systems. *Philos. Trans. R. Soc. Lond. A* **1972**, *272*, 47–78. [CrossRef]
6. Hassanizadeh, S.M.; Gray, W.G. Thermodynamic basis of capillary pressure in porous media. *Water Resour. Res.* **1993**, *29*, 3389–3405. [CrossRef]
7. Cannon, J.R. The solution of the heat equation subject to the specification of energy. *Q. Appl. Math.* **1963**, *21*, 155–160. [CrossRef]
8. Dehghan, M. Efficient techniques for the second-order parabolic equation subject to nonlocal specifications. *Appl. Numer. Math.* **2005**, *52*, 39–62. [CrossRef]
9. Beshtokov, M.K. Finite-difference method for a nonlocal boundary value problem for a third-order pseudoparabolic equation. *Differ. Equ.* **2013**, *49*, 1134–1141. [CrossRef]
10. Beshtokov, M.H. On a nonlocal boundary value problem for a third-order pseudo-parabolic equation. *Comput. Math. Model.* **2016**, *27*, 60–79. [CrossRef]
11. Beshtokov, M.K. Difference method for solving a nonlocal boundary value problem for a degenerating third-order pseudo-parabolic equation with variable coefficients. *Comput. Math. Math. Phys.* **2016**, *56*, 1763–1777. [CrossRef]
12. Sapagovas, M.; Štikonas, A.; Štikonienė, O. ADI method for pseudoparabolic equation with nonlocal boundary conditions. *Mathematics* **2023**, *11*, 1303. [CrossRef]
13. Huntul, M.J.; Dhiman, N.; Tamsir, M. Reconstructing an unknown potential term in the third-order pseudo-parabolic problem. *Comput. Appl. Math.* **2021**, *40*, 140. [CrossRef]
14. Dhiman, N.; Tamsir, M.; Aldwoah, K.A.; Almalahi, M.A.; Adel, W. Numerical approximation of the 3rd order pseudo-parabolic equation using collocation technique. *Bound. Value Probl.* **2024**, *2024*, 154. [CrossRef]
15. Meetei, M.Z.; Tamsir, M.; Singh, M.; Dhiman, N.; Khan, F.A. A new uniform hyperbolic polynomial B-spline computational scheme for 3rd-order pseudo-parabolic problem. *Mathematics* **2026**, *14*, 542. [CrossRef]
16. Ewing, R.E. Time-stepping Galerkin methods for nonlinear Sobolev partial differential equations. *SIAM J. Numer. Anal.* **1978**, *15*, 1125–1150. [CrossRef]
17. Arnold, D.N.; Douglas, J., Jr.; Thomée, V. Superconvergence of a finite element approximation to the solution of a Sobolev equation in a single space variable. *Math. Comp.* **1981**, *36*, 53–63. [CrossRef]
18. Cuesta, C.M.; Pop, I.S. Numerical schemes for a pseudo-parabolic Burgers equation: Discontinuous data and long-time behaviour. *J. Comput. Appl. Math.* **2009**, *224*, 269–283. [CrossRef]
19. Hesthaven, J.S.; Warburton, T. *Nodal Discontinuous Galerkin Methods: Algorithms, Analysis, and Applications*; Springer: New York, NY, USA, 2008. [CrossRef]
20. Cockburn, B.; Shu, C.-W. Runge–Kutta discontinuous Galerkin methods for convection-dominated problems. *J. Sci. Comput.* **2001**, *16*, 173–261. [CrossRef]
21. Bassi, F.; Rebay, S. A high-order accurate discontinuous finite element method for the numerical solution of the compressible Navier–Stokes equations. *J. Comput. Phys.* **1997**, *131*, 267–279. [CrossRef]
22. Arnold, D.N.; Brezzi, F.; Cockburn, B.; Marini, L.D. Unified analysis of discontinuous Galerkin methods for elliptic problems. *SIAM J. Numer. Anal.* **2002**, *39*, 1749–1779. [CrossRef]
23. Cockburn, B.; Shu, C.-W. The local discontinuous Galerkin method for time-dependent convection–diffusion systems. *SIAM J. Numer. Anal.* **1998**, *35*, 2440–2463. [CrossRef]
24. Castillo, P.; Cockburn, B.; Perugia, I.; Schötzau, D. An a priori error analysis of the local discontinuous Galerkin method for elliptic problems. *SIAM J. Numer. Anal.* **2000**, *38*, 1676–1706. [CrossRef]
25. Cheng, Y.; Shu, C.-W. Superconvergence of discontinuous Galerkin and local discontinuous Galerkin schemes for linear hyperbolic and convection–diffusion equations in one space dimension. *SIAM J. Numer. Anal.* **2010**, *47*, 4044–4072. [CrossRef]
26. Yan, J.; Shu, C.-W. A local discontinuous Galerkin method for KdV type equations. *SIAM J. Numer. Anal.* **2002**, *40*, 769–791. [CrossRef]
27. Xu, Y.; Shu, C.-W. Local discontinuous Galerkin methods for high-order time-dependent partial differential equations. *Commun. Comput. Phys.* **2010**, *7*, 1–46. [CrossRef]
28. Wang, H.; Shu, C.-W.; Zhang, Q. Stability and error estimates of local discontinuous Galerkin methods with implicit–explicit time-marching for advection–diffusion problems. *SIAM J. Numer. Anal.* **2015**, *53*, 206–227. [CrossRef]
29. Gao, F.; Qiu, J.; Zhang, Q. Local discontinuous Galerkin finite element method and error estimates for one class of Sobolev equation. *J. Sci. Comput.* **2009**, *41*, 436–460. [CrossRef]
30. Zhang, Q.; Gao, F. A fully-discrete local discontinuous Galerkin method for convection-dominated Sobolev equation. *J. Sci. Comput.* **2012**, *51*, 107–134. [CrossRef]

31. Zhao, D.; Zhang, Q. Local discontinuous Galerkin methods with generalized alternating numerical fluxes for two-dimensional linear Sobolev equation. *J. Sci. Comput.* **2019**, *78*, 1660–1690. [CrossRef]
32. Abbaszadeh, M.; Dehghan, M. Interior penalty discontinuous Galerkin technique for solving generalized Sobolev equation. *Appl. Numer. Math.* **2020**, *154*, 172–186. [CrossRef]
33. Karniadakis, G.E.; Sherwin, S.J. *Spectral/Hp Element Methods for Computational Fluid Dynamics*, 2nd ed.; Oxford University Press: Oxford, UK, 2007. [CrossRef]
34. Alexander, R. Diagonally implicit Runge–Kutta methods for stiff O.D.E.'s. *SIAM J. Numer. Anal.* **1977**, *14*, 1006–1021. [CrossRef]
35. Hairer, E.; Wanner, G. *Solving Ordinary Differential Equations II: Stiff and Differential-Algebraic Problems*, 2nd ed.; Springer: Berlin/Heidelberg, Germany, 1996. [CrossRef]
36. Xu, Y.; Shu, C.-W. Error estimates of the semi-discrete local discontinuous Galerkin method for nonlinear convection–diffusion and KdV equations. *Comput. Methods Appl. Mech. Eng.* **2007**, *196*, 3805–3822. [CrossRef]
37. Xu, Y.; Shu, C.-W. Superconvergence of local discontinuous Galerkin methods for one-dimensional convection–diffusion equations. *Comput. Struct.* **2009**, *87*, 630–641. [CrossRef]

Disclaimer/Publisher's Note: The statements, opinions and data contained in all publications are solely those of the individual author(s) and contributor(s) and not of MDPI and/or the editor(s). MDPI and/or the editor(s) disclaim responsibility for any injury to people or property resulting from any ideas, methods, instructions or products referred to in the content.